E-150 bis

Proposal for

PLASMA LENS EXPERIMENT AT THE FINAL FOCUS TEST BEAM

April 1, 1997

THE PLASMA LENS COLLABORATION

P. Chen[1*], D. Cline[2*], W. Craddock[1], F. J. Decker[1], R. Iverson[1], T. Katsouleas[3], P. Kwok[2], W. Leemans[4], S. Masuda[2], D. D. Meyerhofer[5], K. Nakajima[6], A. Ogata[6], P. Raimondi[1], A. Sessler[4], D. Walz[1], A. Weidemann[7].

[1]Stanford Linear Accelerator Center, Stanford, California
[2]University of California, Los Angeles, California
[3]University of Southern California, Los Angeles, California
[4]Lawrence Berkeley Laboratory, Berkeley, California
[5]University of Rochester, Rochester, New York
[6]National Laboratory for High Energy Physics (KEK), Tsukuba, Japan
[7]University of Tennessee, Knoxville, Tennessee
[*]Spokesperson

RECEIVED
APR 3 1997

TABLE OF CONTENTS

Summary 1

1. Introduction 3

1.1 Plasma Focusing 3

1.2 Previous Plasma Lens Experiments 4

1.3 Plasma Lens Experiment at the FFTB 6

1.4 Potential Application to an NLC Final Focus 7

1.5 Application to Future Linear Colliders 8

1.6 Other Potential Applications 9

2. Parameter Studies 11

2.1 Simple Model 11

2.2 Transverse Non-linear Effects 12

2.3 Longitudinal Effects 13

2.4 Round Beam Focusing 14

3. Experimental Design 17

3.1 Overview 17

3.2 Plasma Chamber 17

3.3 Laser System 18

3.4 Vacuum System 20

3.5 Beam Size Measurement 21

4. Plasma Formation 23

4.1 Laser Ionization 23

4.2 Plasma Production Test 24

5. Vacuum System 31

5.1 Differential Pumping System 31

Program Summary 35

A. Detector Backgrounds from a Plasma Lens at NLC 37

A.1 Choice of Plasma Lens Parameters 37

A.2 Sources of Backgrounds 39

A.3 Cross Sections and Event Rates 40

A.4 Detector Backgrounds 49

A.5 Summary 52

B. Supersonic Gas Nozzle for Future Plasma Lens Applications 53

B.1 Nozzle Design 53

B.2 Nozzle Fabrication 55

B.3 Initial Operation 56

B.4 Summary 58

References 59

LIST OF TABLES

1. Parameters for Round Beam Focusing.....14
2. Estimated Time Requirement.....35
3. Summary of Background Sources from a Plasma Lens in NLC.....43

LIST OF FIGURES

1. Evolution of Beam Sizes for Case A to C 15
2. Outline of Plasma Lens Experiment at the FFTB 18
3. Isometric View of Plasma Lens Experiment at the FFTB.....19
4. Isometric View of Plasma Chamber.....20
5. Plasma Production Test Apparatus 25
6. PMT Intensity versus Laser Energy at Pressures.....26
7. √PMT Intensity versus Pressure.....27
8. Calibration for PMT Plasma Density Measurement 28
9. Artificially Scaled Image of Plasma 29
10. Differential Pumping System.....32
11. Angular Distributions of the Cross Sections for ep Elastic Scattering.....44
12. Angular Distributions of the Cross Sections for ep Inelastic Scattering.....46
13. Angular Distributions of the Compton Cross Sections from Photon Sources.....48
14. Supersonic Gas Nozzle Design Prior to Extrusion 55
15. Transverse Density Profile of Supersonic Gas Jet.....57

SUMMARY

We propose a plasma lens experiment at the Final Focus Test Beam (FFTB) facility of the Stanford Linear Accelerator Center. This experiment would allow the examination of plasma focusing devices for particle beams in the parameter regime of interest to future high energy colliders. It is expected to lead to compact plasma lens designs capable of focusing the beam to unprecedented small spot sizes. Here we present a revised and simplified proposal which reflects the pertinent scientific and technological advances since the previous proposal[1] was submitted. Also included is a new schedule for the experiment.

CHAPTER ONE

INTRODUCTION

Plasma focusing devices are compact, simple, and very strong focusing elements. The focusing strengths for typical parameters are equivalent to focusing magnets with gradients of 10^9 Gauss/cm. In principle, such strong fields are capable of focusing beams to very small spot sizes[2-7] and perhaps even capable of avoiding[8] the inherent (Oide) limitation[9] in discrete strong focusing. Several proof-of-principle experiments using low density particle beams have demonstrated plasma focusing[10-12]. Our goal is to demonstrate the effectiveness of plasma lenses in the parameter regime of interest for SLC and the next generation of high energy linear colliders. The experience gained is expected to yield new final focus designs capable of generating spot sizes smaller than ever produced before.

1.1 Plasma Focusing

For our purposes, the focusing nature of the interaction can be understood using the following arguments without detailed mathematical analysis: The beam particles carry charge and current. For a relativistic beam in vacuum the electric repulsion is almost neutralized by the magnetic attraction among the particles. The introduction of the beam into the plasma results in a response that nearly neutralizes the intrusion. The charge neutralization takes place primarily by the fast motion of the plasma electrons and current neutralization occurs due to the development of the "return current" in the plasma. The resulting large electric and magnetic fields serve to both accelerate and focus trailing

particles[13]. For a single bunch the head can excite the plasma and focus the main body of the bunch[2].

Underdense Regime: In the regime where the plasma density is lower than the beam density (referred to as "underdense" regime in the literature), the plasma electrons respond to the incoming beam by total rarefaction from the beam volume. The result is a near uniform focusing of the beam due to the less mobile ions.

Overdense Regime: The "overdense" regime corresponds to the case when the plasma density is higher than the beam density. For transverse beam sizes smaller than the oscillation amplitude of the plasma electrons (the plasma wavelength λ_p) the return current flows essentially outside the beam envelope and is ineffective in neutralizing the beam current. Yet, the beam charge is completely neutralized. This leaves the beam azimuthal magnetic field unbalanced, resulting in a pinch, or focusing of the beam. The focusing force varies according to the variation of the beam profile.

Field-Compensation Regime: In the extreme overdense (total compensation) situation, the plasma density is much higher than the beam density, and the return current penetrates deep inside the beam. In this limit the beam magnetic field is also neutralized, and plasma focusing diminishes. This limit is the basis for the concept of "plasma beamstrahlung suppression"[3,14].

1.2 Previous Plasma Lens Experiments

Three low energy, low density beam experiments were performed at Argonne National Laboratory[10], Tokyo University[11], and University of California at Los Angeles[12] which confirm the theory of the beam-plasma interaction. All three

experiments were limited to the overdense plasma lens regime ($n_p > n_b$), with plasma electron densities of order 10^{11} cm^{-3} to 10^{13} cm^{-3}.

In the ANL experiment[10], a 21 MeV electron beam with $2.5 - 4 \times 10^{10}$ particles per bunch was sent through a 35 cm thick plasma which was created in a hollow cathode arc and had a density of $0.7 - 7 \times 10^{13}$ cm^{-3}. The size of the beam was seen to decrease from $\sigma = 1.4$ mm without plasma to $\sigma = 0.9$ mm with plasma, roughly the predicted "Bennett" equilibrium size in a long plasma. The beam size was thought to have been as much as 3 times smaller before reaching the equilibrium size, but unfortunately there was no measurement of the beam size at intermediate positions in the plasma.

In the Tokyo University experiment[11], an 18 MeV round electron beam was sent through a 20 cm long thin plasma lens with a focal length of about 1.5 m. The beam density was about 1.2×10^{10} cm^{-3} and the plasma, which was created before the passage of the electron bunch by a current discharge, had a density of order 10^{11} cm^{-3}. The beam size was measured at three phosphor screens along a drift beyond the plasma lens, and was seen to decrease by about 20% in the presence of the plasma.

Recently at UCLA[12], a 3.5 MeV electron bunch was focused from $\sigma = 2.5$ mm to $\sigma = 0.6$ mm using an overdense thick plasma lens with a focal length of about 20 cm. The 8 cm long plasma was created by RF discharge and had a density of about 5×10^{12} cm^{-3}. The beam size was measured with phosphor screens before and after the plasma lens. Time-resolved measurement of the particle bunch was performed by imaging the Cêrenkov light from a 500 mm thick fused-silica radiator onto a 100 μm slit of a streak camera. The measurements agree well with theory[13,15].

1.3 Plasma Lens Experiment at the FFTB

While previous experimental results have been useful, the beam densities involved in the ANL, Tokyo University, and UCLA experiments were 6 to 7 orders of magnitude lower than the nominal colliding beam density at the SLC/SLD and those expected for next generation linear colliders. The experiments are insufficient to design or evaluate a plasma lens in a high energy collider detector. Systematic evaluation of methods and techniques using realistic high energy and high density beams is required.

A facility such as the FFTB offers a unique environment to test all aspects of plasma focusing for high energy, low emittance beams. In our original proposal[1] we intended to test plasma focusing with both round and flat beams. In the latter case, the intention was to demonstrate a focused beam size which would be even smaller than that achieved by the FFTB. We do believe that the plasma lens can indeed deliver such an unprecedented beam size at the FFTB. With that in mind we propose to test the plasma focusing of round beams and concentrate on demonstrating the power of a plasma lens through its demagnification power, as a first step of experimentation.

We propose to perform a round beam focusing experiment at the FFTB. It would utilize the round beam aspect ratio of $\varepsilon_{nx} = \varepsilon_{ny} = 3 \times 10^{-5}$ m-rad from the FFTB[16], and a charge of 10^{10} particles per bunch. The plasma lens would have electron densities adjustable from 10^{16} to 10^{18} cm^{-3} and a thickness of 3 mm. The plasma will be generated by laser ionization immediately prior to the arrival of the beam. With optimized conditions, the plasma lens will be capable of demonstrating the focusing of a 5 μm round beam to a final spot size of less than 2 μm in both dimensions, or a luminosity enhancement factor of about 10. The simplicity and economy of such a scheme will prove the plasma lens to be a worthy add-on device for luminosity enhancement in linear colliders[7].

1.4 Potential Application to an NLC Final Focus

The Next Linear Collider (NLC) calls for a colliding beam with a bunch population $N = 0.65 \times 10^{10}$, beam dimensions $\sigma^*_{x0} = 300$ nm, $\sigma^*_{y0} = 3$ nm, and $\sigma_z = 100$ μm. The beam density at the IP is $n_{b0} \cong 4.6 \times 10^{21}$ cm^{-3}. The beta functions are $\beta^*_{x0} = 1$ cm, $\beta^*_0 = 100\mu m$. We can envision placing a plasma lens with a density $n_p = 2 \times 10^{18}$ cm^{-3}, and thickness $\ell = 3$ mm, at a distance $s_0 = -1$ cm upstream from IP. The beam density at the entrance of the plasma lens is $n_{b0} \cong 3.2 \times 10^{19}$ cm^{-3}. Calculations (see Appendix A) show that this would reduce the beam optics by $\beta^*_x / \beta^*_{x0} \approx 1/8$ and $\beta^*_y / \beta^*_{y0} \approx 1/5$. Since the beam size scales as $\sqrt{\beta^*}$, this corresponds to an enhancement of luminosity by a factor $\sqrt{\beta^*_{x0}\beta^*_{y0} / \beta^*_x\beta^*_y} \approx 6$. We emphasize that as the colliding beams become tighter, there is yet an additional gain of luminosity through the strong beam-beam disruption (pinching) effect. Thus, there is a "bootstrapping" effect induced by the plasma lens[5], and the net enhancement of luminosity will be larger than the stated pure geometric factor of six. Note that the plasma lens parameters in this example fall in the same range as that in our proposed experiment at the FFTB. Thus the results of our experiment should be directly applicable to NLC.

However, the issue of plasma lens induced high energy detector backgrounds casts a shadow of doubt regarding the ultimate utility of plasma lenses in high energy physics. Sharing this concern, we have carried out a systematic effort to estimate the plasma lens induced backgrounds in different components of a hypothetical NLC detector (modeled after SLD). With a rather conservative approach, the yields, calculated per train of 90 bunches within a total time span of approximately 125 ns, appear to be marginal for the drift chamber. The backgrounds for other components are within the tolerances[17]. Details of the study on backgrounds are reported in Appendix A.

It should be noted that with rapid advances in computer and data processing techniques, it appears reasonable to have the time resolution in a future NLC detector be much shorter than 125 ns. In the extreme case it can be envisioned that the events can be registered per bunch, with a time-resolution of about 1.5 ns[18]. In such a scenario the detector should remain clean with the insertion of the plasma lens (see Appendix A).

We note that these background calculations are based on the assumption that there is no excessive hardware (such as a plasma chamber) surrounding the IP. Implicitly, we realize that a better design of a plasma lens for a realistic high energy application should employ a supersonic gas nozzle instead of a plasma chamber of the type proposed herein. We have devoted research and development efforts to a gas nozzle suitable for plasma lens applications with encouraging results. Details of these efforts are reported in Appendix B.

In summary, we believe that the plasma lens should help as a booster to enhance the NLC luminosity either beyond its design value, or to improve the luminosity in the event the machine fails to perform up to its design criterion. It should be mentioned that in addition to luminosity enhancement in the e^+e^- collision mode, the plasma lens can, in principle, be used to divert the spent e^- beams in the $\gamma\gamma$ collision mode[19]. One other possible application in linear colliders is that a plasma lens can help to stabilize[20] the (inherently unstable) e^-e^- collision, if so desired.

1.5 Application to Future Linear Colliders

There are research activities toward a multi-TeV future linear collider beyond the energy reach of NLC. These activities aim at acceleration gradients much higher than the X-band (of order 100 MeV/m) level to be employed in NLC. The goal is to significantly reduce the length of the accelerator. It is well-known that in a linear collider the beam

collimation (BC) and the final focus (FF) sections are essential to the delivery of small beam size at the IP. This demands very extended lengths of beam line (a few kilometers in NLC). It is therefore highly desirable to significantly reduce the lengths of BC and FF systems via novel concepts. Indeed, the potential reward from this direction of research should be no less than that from the ultra-high acceleration gradient developments.

In addition to the super-strong focusing available from a plasma lens, which could help to reduce the FF length, it was recently suggested[21] that a plasma can serve to collimate the beam phase space distribution tail. If realized, it would help to greatly reduce the length of the collimation section in a linear collider. When a high intensity beam traverses a neutral gas, the core of the beam carries such a strong electromagnetic field that the gas will be instantly (tunneling) ionized into a plasma. This plasma would then provide strong focusing on the core part of the beam whereas the particles on the fringe are unaffected. Such a difference in optics will provide a means for the tail particles to be separated from the core downstream. Such a novel approach would, in principle, greatly reduce the length of the BC section in future linear colliders.

1.6 Other Potential Applications

In a totally different environment, it was shown[22] that a plasma lens can help suppress the beam-beam tune-shift in circular colliders. In the self-focusing regime of beam-plasma interaction, the plasma response to the incoming beam is to neutralize the beam space charge and the electric field of the beam is largely canceled. When the plasma density is much higher than that of the beam, the plasma "return current" penetrates into the beam volume. In the limit, the magnetic field of the beam is largely suppressed as well, and the beam-beam interaction (the beam-beam tune-shift) diminishes. This in turn can help to

increase the beam current, and therefore the collider luminosity. Indeed, this is Case C of the plasma lens experiment which we propose to study (see Chapter 2).

In summary, there is a wide range of potential applications of plasma lenses in high energy physics[23].

CHAPTER TWO

PARAMETER STUDIES

The prospect of testing plasma lens concepts at the FFTB was investigated[24]. In the study, plasma lens parameters for round beam focusing, flat beam focusing, and "adiabatic focusing"[8] were provided. Here we refine our treatment and limit ourselves to round beam focusing only. We consider beam energies of 50 and 30 GeV, which are the current configuration of the accelerator and its future configuration as PEP II (B factory) injector, respectively. In either case, the effectiveness of the plasma lens can be demonstrated.

2.1 Simple Model

When ignoring the effects due to the return current, the focusing strength K for underdense plasma lenses is governed by the plasma density n_p,

$$K = \frac{2\pi r_e}{\gamma} n_p \ , \tag{2.1}$$

where r_e is the classical electron radius and γ is the relativistic kinetic energy factor of the beam. For overdense plasma lenses the strength is determined by the beam density n_b,

$$K = \frac{2\pi r_e}{\gamma} n_b \ . \tag{2.2}$$

The plasma return current tends to reduce the focusing effect of the lens [14]. The effect is approximately given by

$$K_{rc} = \frac{K}{1+(k_p\sigma_r)^2} \ , \tag{2.3}$$

where σ_r is the rms size of the beam and $k_p = \sqrt{4\pi r_e n_p}$ is the plasma wave number. The effect is appreciable only when the plasma is considerably denser than the beam.

The response of the plasma occurs in a time $\tau_p = 1/\omega_p$ and therefore in the overdense regime the requirement for response within the time of a beam pulse is $\tau_p \ll \tau_b \sim \sqrt{2\pi}\sigma_z$, or $k_p\sigma_z \gg 1/\sqrt{2\pi}$, where σ_z is the rms bunch length. In the underdense regime, the wave breaking limit is quickly reached and the focusing is less subjected to the limit.

2.2 Transverse Non-linear Effects

Plasma focusing is self-induced, which usually results in the outer edges of the bunch not experiencing the same focusing as the core. Such an effect can, however, be ignored for all underdense cases when the plasma perturbation is beyond the wave breaking limit. However, when the plasma is overdense the focusing field follows roughly the fields in the beam and the non-linear effect is not negligible. Models that treat the aberrations due to such non-linearities in plasma focusing have been developed[4,6]. In the model developed by Rosenzweig and Chen[3], an aberration power is introduced to be

$$P = [1 + (\frac{\beta_0}{f}\delta)^2]^{1/2} , \tag{2.4}$$

where β_0 is the beta function at the lens entrance, f is the focal length for a bi-Gaussian bunch, and $\delta^2 \approx 0.15$ is the parameter for the bi-Gaussian distribution. The reduction in spot size is then given by

$$\frac{\beta^*\varepsilon}{\beta_0\varepsilon_0} = \frac{P^2}{P^2 + (\alpha_0 + \frac{\beta_0}{f})^2} , \tag{2.5}$$

where α_0 and β_0 are the initial Twiss parameters and ε_0 is the initial emittance.

Another transverse effect already mentioned is the weakening of focusing due to the return current. The current flows outside the bunch (e^- beam) and only at high plasma densities does it penetrate the bunch and dilute the focusing due to charge neutralization. Otherwise the focusing is weakened only for some outer particles while most of the particles are in the interior. So the effect can be ignored in all cases except in the field-compensation regime.

2.3 Longitudinal Effects

The focusing strength of a plasma lens is derived from the plasma response to the beam fields which directly depend on the beam density. Generally the focusing strength should be governed by the plasma density in the underdense regime, and by the beam density in the overdense regime, as seen in (2.1) and (2.2). Normally, the beam density has a longitudinal profile which may be modeled reasonably by a Gaussian distribution. Therefore, in the overdense regime the focusing strength varies according to such a beam density profile. Even in the underdense regime, because of the Gaussian variation of the beam density, the head of the beam will always be less dense than the plasma, and the focusing strength turns constant only behind the crossover point where the beam density and the plasma density become equal.

To elucidate the longitudinal effects, we perform the calculations discussed in Section 2.1 with the focusing strength varied locally along the beam according to the relative beam and plasma densities. In our model calculations, the focusing strength switches between (2.1) and (2.2) at $n_p/n_b = 2$, since particle-in-cell simulations indicate that the plasma perturbation is already violent and the wave breaking limit is reached at this value. Furthermore, simulations also show that once wave breaking is reached the near

uniform focusing is retained throughout the remainder of the beam, even though the situation returns to the overdense regime near the tail.

2.4 Round Beam Focusing

We envision that the FFTB emittance is adjusted to a round beam configuration of $\varepsilon_{nx} = \varepsilon_{ny} = 3 \times 10^{-5}$ m-rad for a bunch population of 10^{10}. With the relaxed beam properties, many of the chromatic corrections at the FFTB can be less stringent as well. A laser ionized plasma with a thickness of 3 mm and adjustable plasma density from 10^{16} to 10^{18} cm^{-3} is placed at a distance of 2 mm from the vacuum focus.

Beam Parameters	Case A		Case B		Case C	
E_0 [GeV]	30	50	30	50	30	50
N [10^{10}]	1	1	1	1	1	1
ε_n [10^{-5} m-rad]	3.0	3.0	3.0	3.0	3.0	3.0
β_0^* [mm]	45	75	45	75	45	75
σ_{r0}^* [μm]	4.74	4.74	4.74	4.74	4.74	4.74
β_0 [mm]	48.1	80.3	48.1	80.3	48.1	80.3
σ_0 [μm]	4.91	4.91	4.91	4.91	4.91	4.91
σ_z [mm]	0.47	0.47	0.47	0.47	0.47	0.47
n_{b0} [10^{16} cm^{-3}]	5.3	5.3	5.3	5.3	5.3	5.3
Lens Parameters						
n_p [10^{16} cm^{-3}]	2	2	10	10	100	100
$k_p\sigma_z$	12.5	12.5	28	28	88.5	88.5
s_0 [mm]	-20	-20	-20	-20	-20	-20
ℓ [mm]	3	3	3	3	3	3
f [mm]	22.8	47	17.4	35.7	21.6	36
Focused Beam						
β_r^* [mm]	22.2	37	12.6	21	20.4	34
σ_r^* [μm]	2.01	3.35	1.53	2.55	1.94	3.23
s^* [mm]	2.8	28.5	-2.6	10.7	1.6	17.5

Table 1: Parameters for Round Beam Focusing.

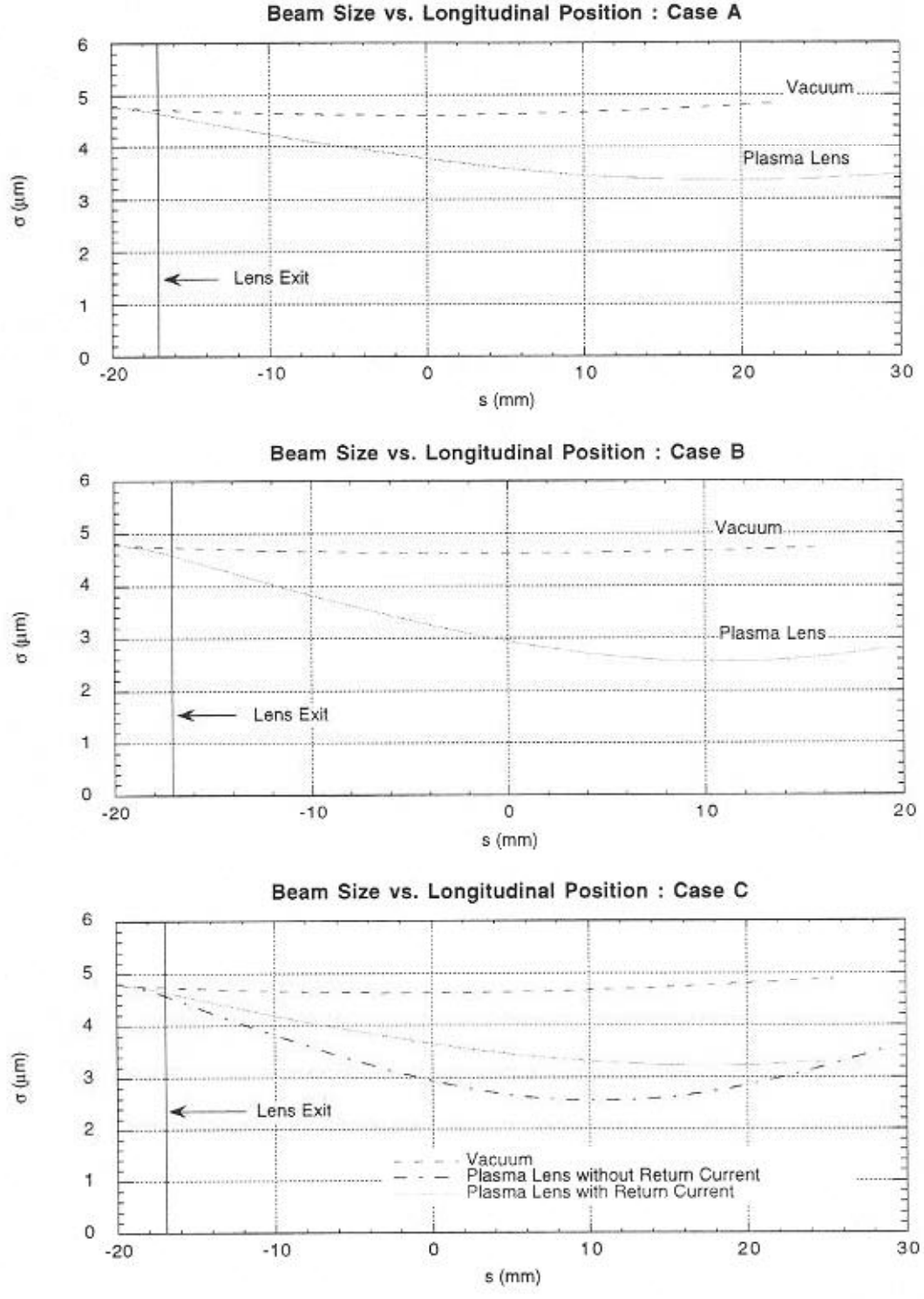

Figure 1: Evolution of Beam Sizes for Case A to C.
Beam energy of 50 GeV is assumed.

Parameters for three typical cases with different plasma densities are shown in Table 1. Here, E_0 is the beam energy, N is the number of particles per bunch, ε_n is the normalized emittance, and the bunch length is σ_z. The focused beam size in vacuum is σ_{r0}^* with corresponding beta function β_0^*. The density of the plasma lens is n_p, and the focal length is $f = s^* - s_0 - \ell/2$, where s^* is the distance of the new focal point from that of the vacuum, ℓ is the lens thickness, and s_0 is the location of the entrance to the plasma lens with respect to the vacuum focal point. At the entrance to the plasma lens, the beam size, beta function, and beam density are σ_o, β_o, and n_{bo}, respectively. The evolution of the integrated beam sizes in cases A through C are plotted as Figure 1. The effects of the longitudinal variation are included in the calculation.

In Case A, an underdense plasma lens with $n_p = 2 \times 10^{16}$ cm^{-3} focus the beam from about 5 μm to 3.4 μm and to 2.0 μm, for 50 GeV and 30 GeV beams, respectively. Increasing the plasma density to 10^{17} cm^{-3}, as shown in Case B, allows the study of overdense plasma focusing without degradation due to return currents. In this case, the plasma focusing is strongest in this experiment, and the beam size decreases from 5 μm to 2.6 μm and to 1.5 μm, for 50 GeV and 30 GeV beams, respectively. In Case C, the plasma is much denser than the beam, and the beam-plasma interaction is in the extreme overdense regime, where the focusing strength diminishes due to return currents. It is important to note that the extreme overdense regime in Case C is the basis for the concepts of "plasma beamstrahlung suppression"[3,14], and "beam-beam tune-shift suppression" in circular colliders[22].

CHAPTER THREE

EXPERIMENTAL DESIGN

The apparatus for the plasma lens experiment is to be installed at Station 1027 on the FFTB[16]. The location is within the final focus region of the FFTB and has ample space available for installation of all accessories. The design is to minimize the impact on the existing FFTB beam line.

3.1 Overview

The arrangement consists of a plasma chamber sandwiched between two identical differential pumping systems, and has ports for ionization laser, plasma diagnostics, gas supply, and beam size measuring devices. The ionization laser is the same 1 μm wavelength laser system as was used for the non-linear Compton scattering experiment (E-144) at the FFTB[25]. A small portion of the laser will be doubled in frequency for plasma diagnostics using Thomson scattering. Conventional wire scanners will be used for all beam size measurements. Hydrogen gas will be used as the plasma source to minimize background radiation from beam-plasma interaction. The outline of the plan and an isometric view of the design are shown as Figure 2 and 3, respectively.

3.2 Plasma Chamber

The design of the plasma chamber (Figure 4) opts for reducing the amount of hardware at the beam-plasma interaction point. The plasma chamber is an 8-port vacuum chamber of sufficient internal transverse size to allow the synchrotron radiation

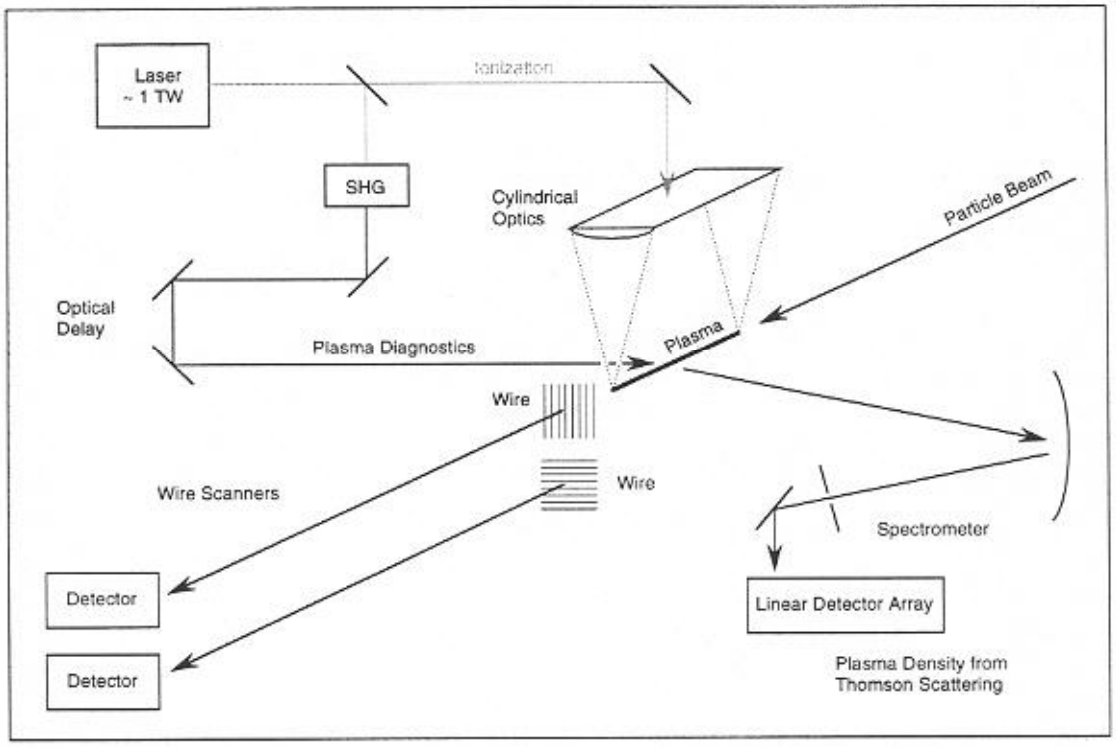

Figure 2: Outline of the Plasma Lens Experiment at the FFTB.

accompanying the particle beam to pass through. Hydrogen gas is transversely supplied to the plasma chamber at a pressure of about 15 torr. The active chamber volume is 25 mm in diameter and 3.5 mm in axial length. It is bounded by two beryllium windows with 1 mm diameter holes for the beam to pass through. Ionization and diagnostic lasers are brought into and out of the chamber through ports on the chamber. The hydrogen gas leaks through the holes in the windows and is pumped off by differential pumping systems on both sides of the plasma chamber.

3.3 Laser System

The ionization laser pulse for the experiment will be generated by the same 1 μm wavelength laser system which was developed for experiment E-144[25]. The high-power

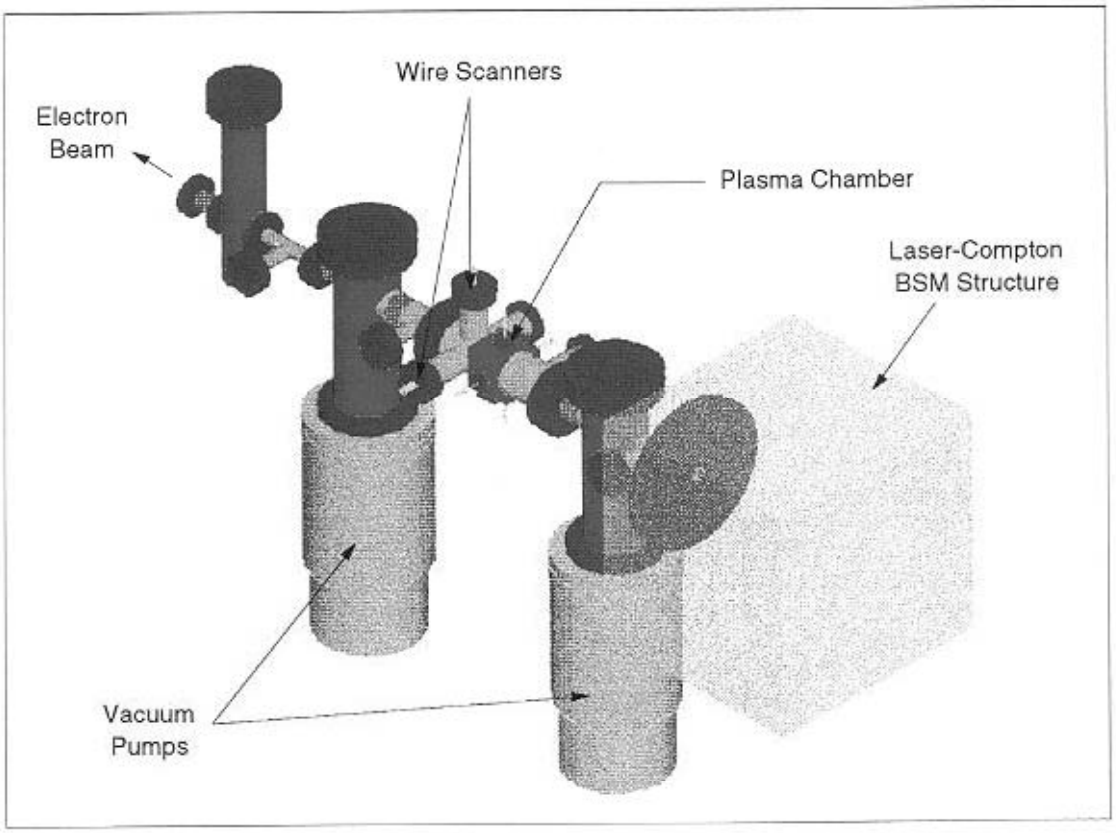

Figure 3: Isometric View of Plasma Lens Experiment.

Nd:glass laser is based on the concept of chirped pulse amplification and compression (CPA)[26-29], which produces pulses of 1 ps duration with energies up to 2 J at 1 Hz. The laser is synchronized to the electron beam with an accuracy of approximately 1 ps.

The laser pulses will be transported to the plasma chamber by an extension of the current laser transport system to the E-144 IP1 region. The upper mirror box of the existing optical transport system has additional ports built in which can accommodate the plasma lens experiment. Less than 15 m of new laser beam transport will need to be installed.

The bulk of the laser energy will be focused with a cylindrical lens to form the plasma lens. A small portion of the laser energy will be split off and frequency doubled to provide a 0.5 μm wavelength pulse for plasma diagnostics[30].

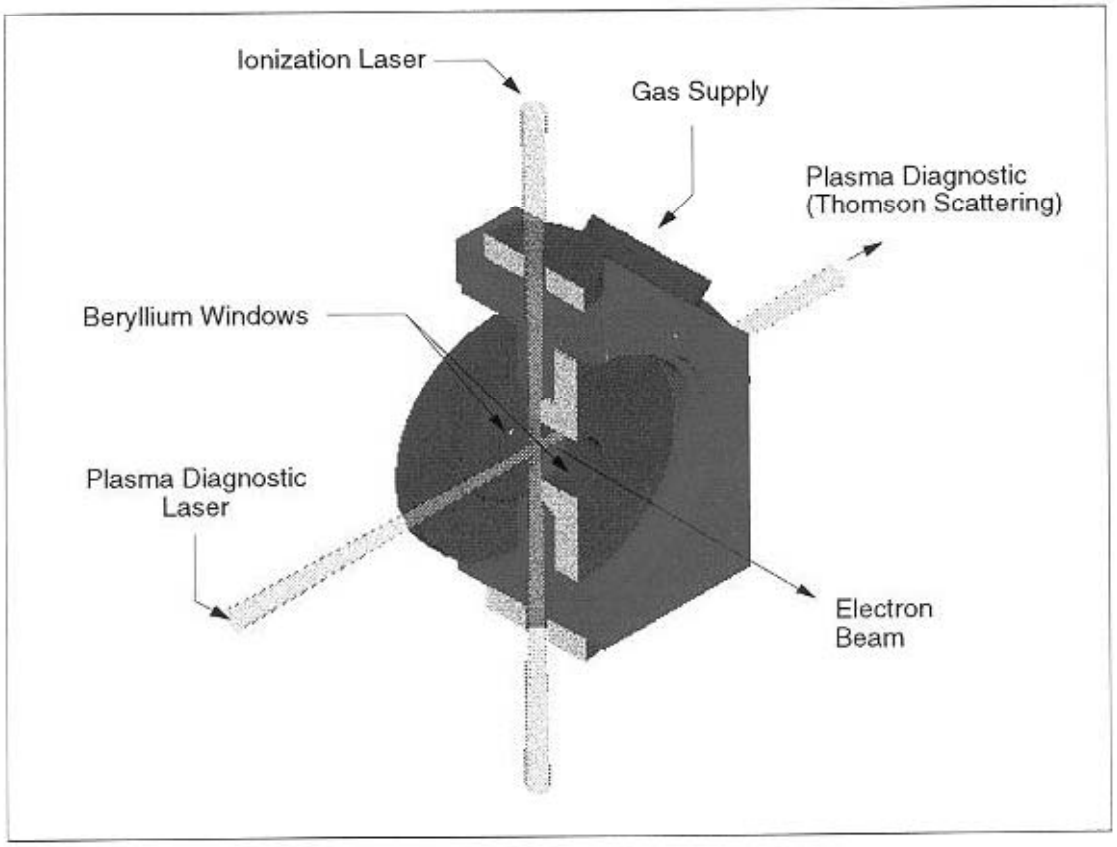

Figure 4: Isometric View of the Plasma Chamber.

3.4 Vacuum System

Differential pumping systems are used on both sides of the plasma chamber to handle the gas load on the FFTB beam line from the plasma lens leaking through the holes in the beryllium windows. Most of the gas will be collected through the first stage pump outs on either side of the plasma chamber. The remaining stages will handle the gas that escaped the first stage and diffused into the beam line. Additional windows with small apertures will separate the pumping stages for increased vacuum performance. A pressure of order 10^{-6} torr can be reached at the end of the third stage. The small quantities of hydrogen involved will not pose a safety problem for the scheme. The FFTB beam line is connected to the linear accelerator via a section of beam transport in the beam switch yard

(BSY). Therefore, loss of power to the vacuum pumps in the differential pumping system or other pump failures could potentially allow hydrogen gas to contaminate a large part of this vacuum system. To guard against such failures, we propose to isolate the plasma cell experimental region by installing two solid beryllium windows (~25 μm thick). These windows would be captured in vacuum flanges. The upstream one is just ahead of the laser-Compton interferometer beam size monitor and the downstream one is just ahead of the first FFTB dump line quadrupole magnet QP1A. These are locations where the transverse beam size is large enough that such windows can survive indefinitely.

3.5 Beam Size Measurement

For the experiment, the spot sizes involved are within the range of wire scanners[31]. The spot sizes are determined from the bremsstrahlung yields as the electron beam is scanned across micron-sized fibers.

The focal point wire scanner presently in the FFTB will be replaced. The new device will be integrated mechanically with the plasma chamber, but will make use of carbon fibers of the same 4 μm nominal diameter as the present scanner. The equipment in the FFTB has frequently measured beam spot sizes with σ_y less than 1 μm, making use of as few as six samples across the beam profile.

The limiting systematic uncertainty in these measurements has been the knowledge of the diameter of the carbon fiber being scanned. Note that the rms width of a 4 μm diameter wire is 1 μm, which is the number that enters in quadrature with the Gaussian width of the beam. If the wire diameter is known to ±5%, and the beam size is, for example, 2 μm, then the uncertainty in the spot measurement from this source is ±1%.

The bremsstrahlung signal is detected by a set of γ-ray and electron detectors downstream. The results from these counters are cross-checked against each other, and in normal FFTB operations they agree well. The ratio of peak signals expected from a scan of the fiber, relative to the bremsstrahlung from the injected gas, is better than 100:1. Wire scanners have been used successfully with signal-to-noise ratios of 1:1. The high signal-to-noise ratio obtainable with wire scanners should convey rather high immunity to the beam-plasma background noise.

The carbon fibers have a rather sharp beam intensity limit. The abruptness is caused by energy loss of the beam in the fiber leading to overheating after a single beam pulse. It is found that, for intensities of 10^{10} electrons per pulse, a spot defined by $\sigma_x \times \sigma_y < 3\ \mu m^2$ will break a carbon fiber. The limiting beam spot area varies inversely with the beam intensity, which impose a constraint on the accessible spot sizes and beam flux in the experiment.

CHAPTER FOUR

PLASMA FORMATION

The plasma density required for meaningful lens tests at the FFTB is in the range of 10^{16} to 10^{18} cm^{-3} over a length of 0.3 cm. In order to meet these requirements we intend to use laser ionization of the gas target to form the plasma using a high-powered laser.

4.1 Laser Ionization

Recent development of high-brightness table top lasers has led to a number of experiments demonstrating plasma formation by laser ionization of a gas[26-29,32]. The technique is attractive because plasma densities can be precisely controlled and reproduced with an accuracy better than a few percent by controlling the pressure of the gas prior to ionization. The length of the plasma can also be controlled by appropriate choice of cylindrical optics to create a line focus of the desired width. Under these conditions, laser ionization occurs primarily by tunneling[27].

The choice of laser parameters is dictated by the plasma requirements. First, hydrogen gas will be used to produce the plasma to limit background radiation caused by bremsstrahlung. Secondly, in order to avoid density clamping due to refraction of the laser by the plasma, a laser wavelength of 1 μm or less should be used[32]. Plasma densities of approximately 5×10^{18} cm^{-3} have been achieved by Darrow *et al.* using a Nd:glass laser at 1 μm[33]. The required intensity to fully ionize molecular hydrogen gas through tunneling ionization is of the order of 10^{14} W/cm^2. Assuming a spot size for the line focused laser beam of up to 50 microns by 3 mm, we require a peak power of 1.5×10^{11} W.

4.2 Plasma Production Test

There have been experiments[26,33] where plasmas with electron densities of order 10^{18} cm^{-3} were produced. However, there was no demonstration of the production of plasmas with extended dimensions at the same densities using transverse laser illumination. The plasma production test serves to confirm that plasmas suitable for the plasma lens experiment at the FFTB can be generated.

The plasma production test was performed at the Laboratory for Laser Energetics of the University of Rochester, New York, in November 1994. The plasma was created using a Nd:glass laser system that is capable of delivering up to 1 J at 1 μm wavelength with a nominal pulse length of 1.3 ps. The high-powered laser system is based on the concept of chirped pulse amplification and compression (CPA)[26-29], and is similar to the one installed and operating at the FFTB for experiment E-144[25].

The plasma density in the test was determined by measuring the emitted recombination light with a photomultiplier tube (PMT)[34]. The intensity of the recombination light is proportional to the square of the plasma electron density[34]. The recombination light was imaged onto a slit before entering the PMT so that the densities at different regions of the plasma can be measured. For the test performed, the slit was positioned at the maximum intensity region so that the peak density of the plasma was measured.

The schematic of the experimental chamber for the test is shown as Figure 5. The chamber has a diameter of about 19.5 cm, and there are three windows for diagnostics. The PMT was mounted at 45° to the direction of propagation of the laser. A CCD camera was positioned perpendicular to the path of the laser to facilitate the measurement of the size of the plasma.

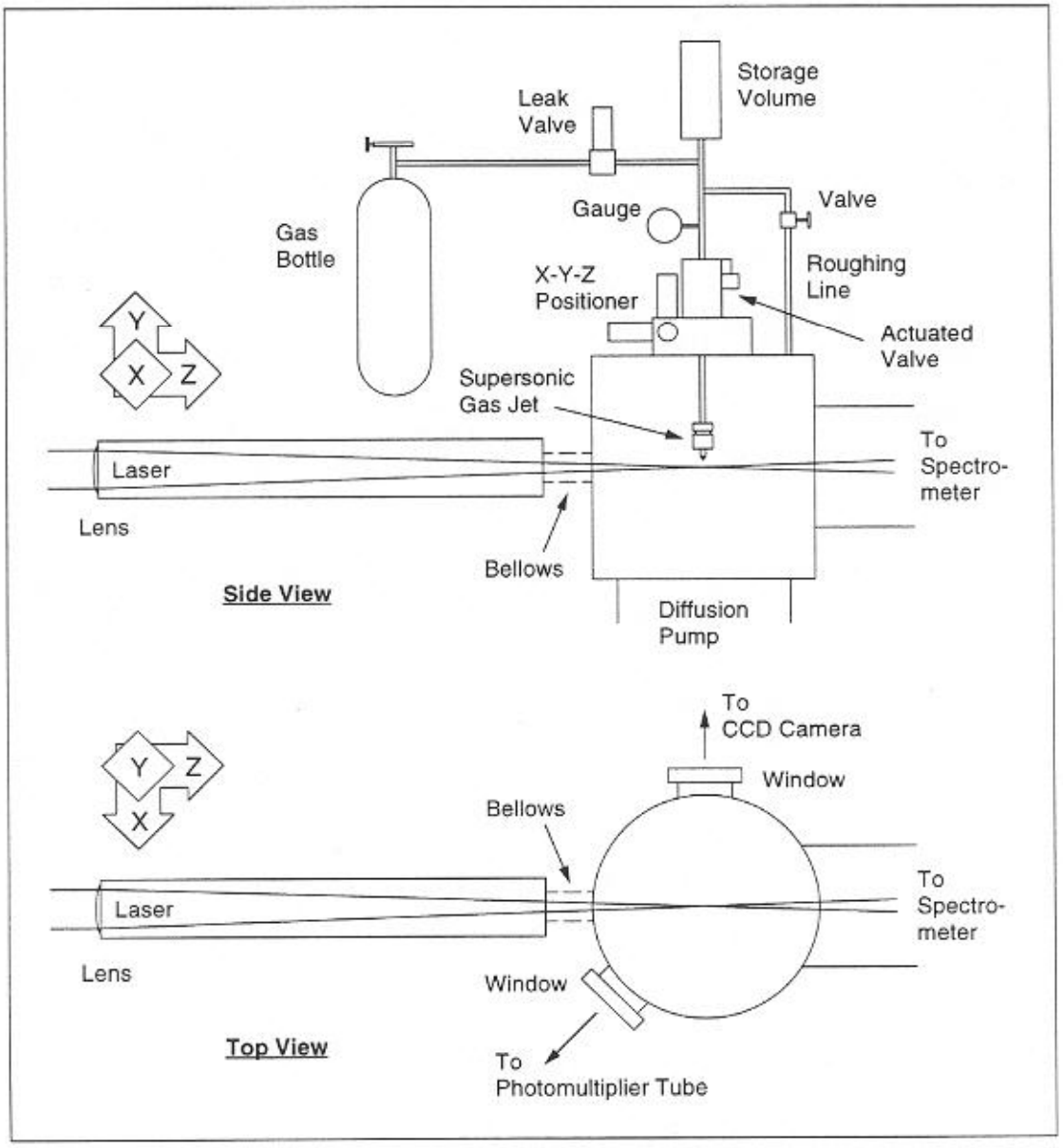

Figure 5: Plasma Production Test Apparatus.

The laser enters the chamber through a port connected to a cylindrical laser beam pipe containing a 1.5 m focal length spherical lens at the far end of the pipe. The nominal focal spot size of the laser was about 100 μm FWHM, which corresponds to a Rayleigh length of approximately 3 mm. The laser energy used for the test was up to 600 mJ. In

order to produce the 1 mm plasma with transverse illumination, a -66 m focal length cylindrical lens was placed just in front of the 1.5 m spherical lens.

The chamber and beam pipe were evacuated by a diffusion pump with a capacity of 300 liters per second.

The experiment was performed in two parts. First, the laser was focused with a spherical lens to calibrate the PMT density measurement and to determine the spatial resolution of the CCD imaging system. After the diagnostics were calibrated, a cylindrical lens was installed to give the laser a transverse line focus approximately 1 mm long.

For safety and availability reasons, the plasma production test was performed with xenon which has ionization potentials similar to hydrogen. The chamber was filled

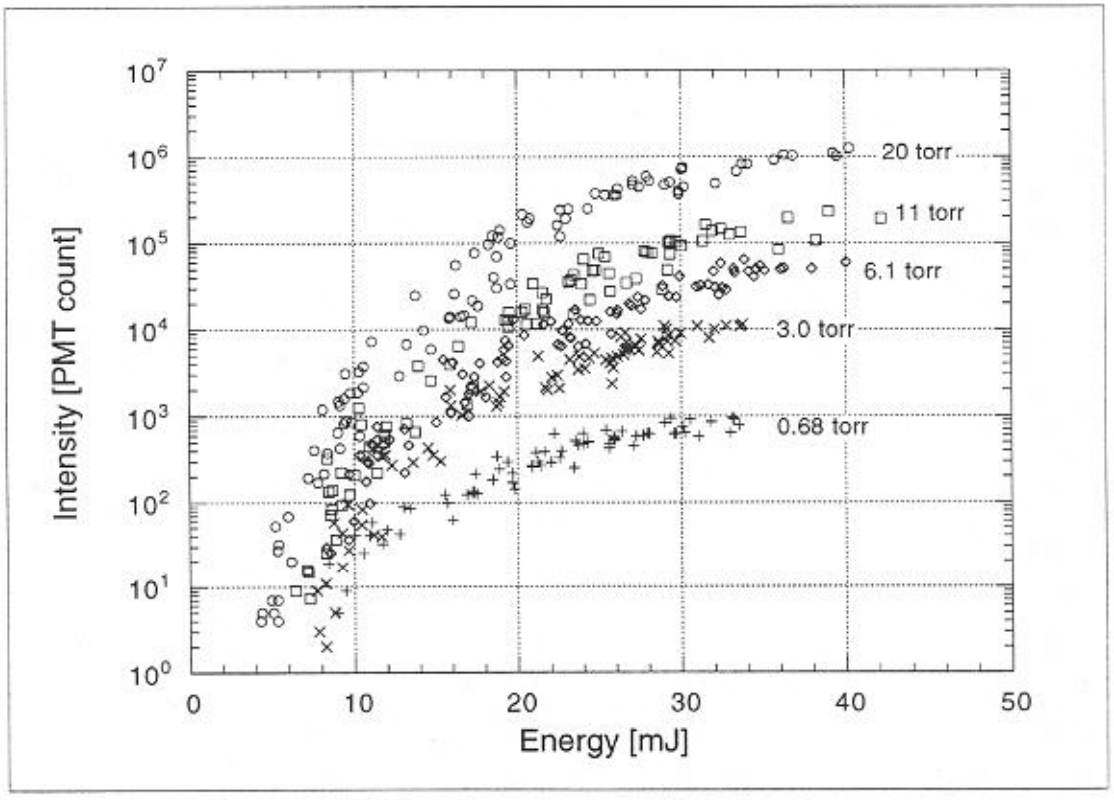

Figure 6: PMT Intensity versus Laser Energy at Pressures.

completely to known pressures of xenon, and plasmas with electron densities of order $10^{18}\,cm^{-3}$ were created.

Since xenon can have multiple charge states, it allowed a lower gas pressure to be used in the chamber to obtain an electron density of 10^{18} cm^{-3}. The lower gas pressure helps to minimize the defocusing of the ionization laser in the xenon filled chamber.

The calibration for the plasma density measurement using a PMT was obtained by filling the chamber with xenon at different known pressures and the intensities of the plasma recombination light were recorded over a range of laser energies.

The PMT intensity versus laser energy at various chamber pressures is plotted as Figure 6. The recombination light intensity begins to saturate for laser energies higher than

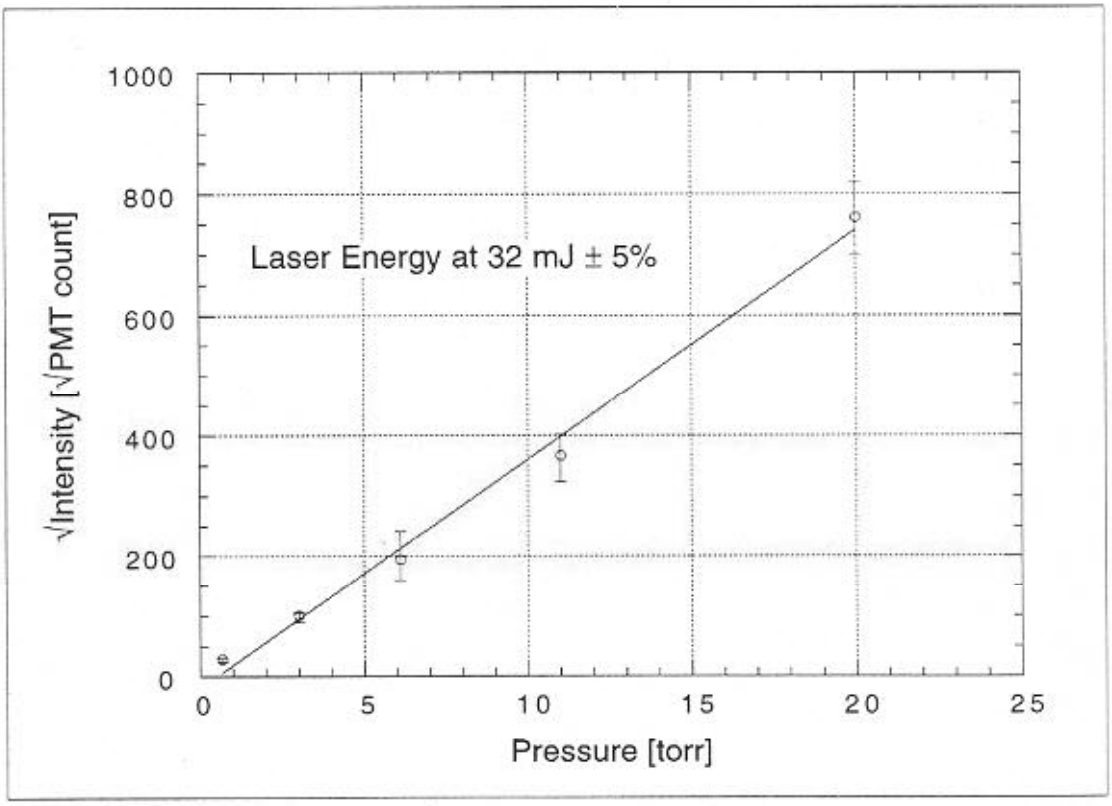

Figure 7: √PMT Intensity versus Pressure.

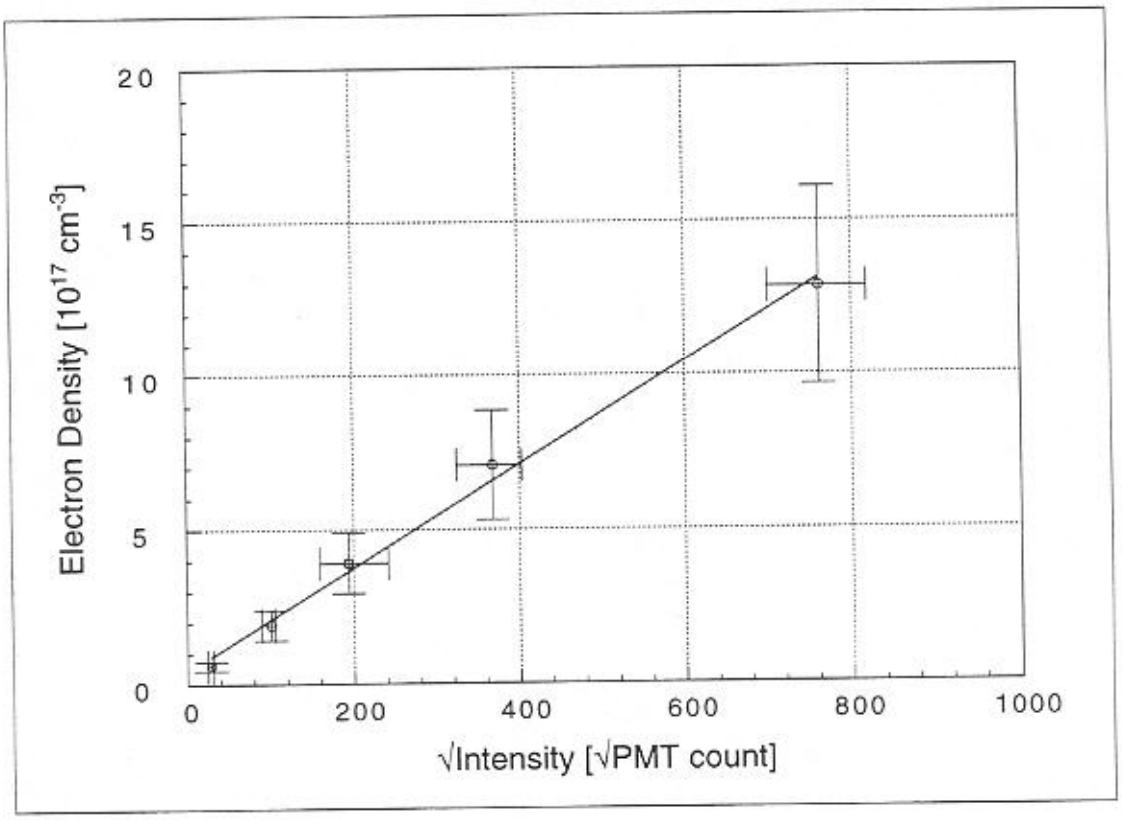

Figure 8: Calibration for PMT Plasma Density Measurement.

30 mJ for all pressures. The intensity changes more slowly with changes in laser energy at energies higher than 30 mJ. The saturation is due to the complete ionization of Xe^{+2} in the focus[27].

The plot of the square root of the PMT signal versus pressure at 32 mJ ± 5% of laser energy is shown as Figure 7. The intensity of the recombination light is proportional to the square of the plasma electron density, and converting pressure into electron density with a factor of 2 for Xe^{+2} gives the calibration for the plasma density measurement using the PMT, as shown in Fig. 8. Error bars are given for charge states between 1.5 and 2.5.

Using the calibrated PMT, the densities of subsequent plasmas produced can be determined. With the chamber filled to 20 torr of xenon, plasmas were created with about

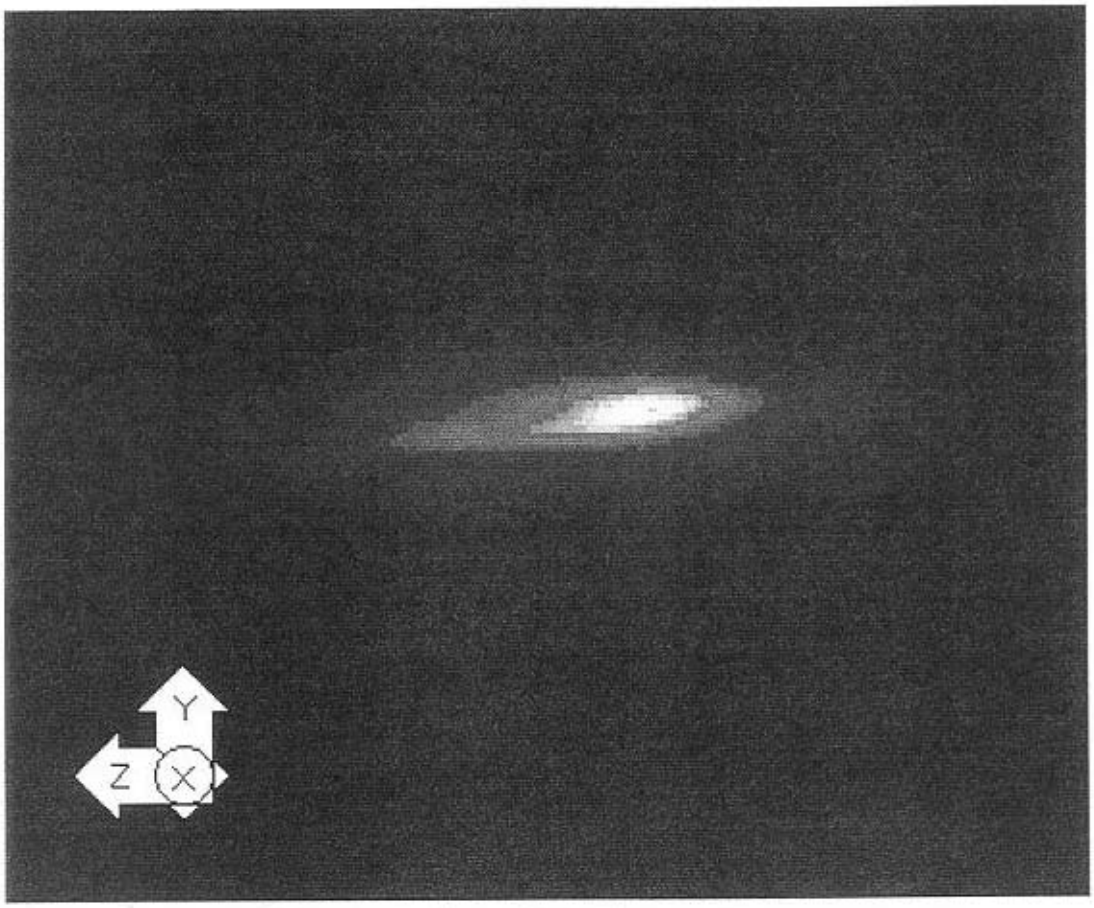

Figure 9: Artificially Scaled Image of Plasma.
The plasma measures over 1 mm FWHM in the Y-dimension.

300 mJ of laser energy. The square root of the averaged PMT count was 760, which indicates that the plasma electron density was of order 10^{18} cm^{-3}. The plasmas had diameters of about 0.7 mm FWHM, as measured by the CCD camera.

The directly measured laser spot size was 100 μm FWHM, whereas the CCD camera measured plasmas with 0.7 mm FWHM, without the cylindrical lens. The spatial resolution of the camera was therefore $\sqrt{(0.7^2 - 0.1^2)} \approx 0.7$ mm.

A -66 m cylindrical lens was installed to create a plasma with a 1 mm transverse size (perpendicular to the laser propagation direction). The transverse size of the line focus

was approximately 100 μm by 1 mm. The long dimension of the line focus was created in the Y-direction (see Figure 9). A 300 mJ laser pulse was focused into the chamber filled with 20 torr of xenon.

Figure 9 shows an artificially scaled image of the plasma in the YZ-plane. It is important to note that the long dimension in the figure is in the Z-direction, which is approximately 1 cm and shows the Rayleigh range associated laser focusing. The transverse image size is approximately 1.3 mm.

The square root of the averaged PMT count was 1,345. Since the transverse dimension with the cylindrical lens is larger than in its absence, the relative sizes of the two plasmas must be considered in determining the electron density. The deconvoluted transverse plasma size with the cylindrical lens was $\sqrt{(1.3^2 - 0.7^2)} \approx 1.1$ mm. The geometric ratio between the cases with and without the cylindrical lens is then 11, and the square root of the averaged PMT count in the case with the cylindrical lens must be reduced by a factor of 3.3.

With the corrections included, the square root of the averaged PMT count for the plasmas produced with the cylindrical lens is approximately 400, which corresponds to a plasma electron density of 0.8×10^{18} cm^{-3}.

The plasma production test has shown that the generation of a plasma with length in excess of 1 mm, and an electron density of order 10^{18} cm^{-3} is feasible using laser ionization.

CHAPTER FIVE

VACUUM SYSTEM

One of the main challenges for a successful plasma lens experiment at the FFTB is a vacuum system to handle the gas load from the plasma lens. The vacuum requirements for the plasma lens experiment are dictated by the plasma density involved and the FFTB beam line vacuum requirement of 10^{-6} torr. The maximum plasma density in the experiment is about 10^{18} cm^{-3} or about 15 torr of hydrogen gas. In addition, vacuum pumps must be nearly vibration free or physically remote from the beam line. A high performance three stage differential pumping system has been designed for the job.

5.1 Differential Pumping System

The calculation of vacuum and pumping requirements is straightforward using formulae from the kinetic theory of gases[35]. Hydrogen escapes through the 1 mm particle beam entrance and exit holes on the beryllium windows at a mass flow rate of 10^{-3} g/s per hole at the maximum pressure of 15 torr within the plasma chamber. Such a gas load will require an unreasonably large pumping speed to evacuate in a single stage to reach 10^{-6} torr. Hence, multistage differential pumping systems are required on both sides of the plasma chamber.

The two differential pumping systems share a common first stage. A 112 l/s Roots pump is used on the first stage to achieve a vacuum of order 10^{-1} torr. The Roots pump is chosen because it can maintain a high pumping speed at higher inlet pressure (up to 1 torr) than can turbo molecular pumps.

The second stages of the pumping systems employ 495 l/s conventional turbo molecular pumps to attain pressures of order 10^{-4} torr. The third stages are equipped with 495 l/s pumps identical to the ones for the second stages. The vacuum at the end of the third stages are of order 10^{-6} torr.

Final solid thin foil beryllium windows on both the upstream and downstream sides of the experiment keep the majority of the FFTB beam line free of hydrogen contamination.

The total pumping speed of the system is rather moderate. In order to have a vacuum of order 10^{-6} torr at the end of the third stage, beryllium windows with 1.5 mm diameter openings are placed at the junctions between stages. The windows have

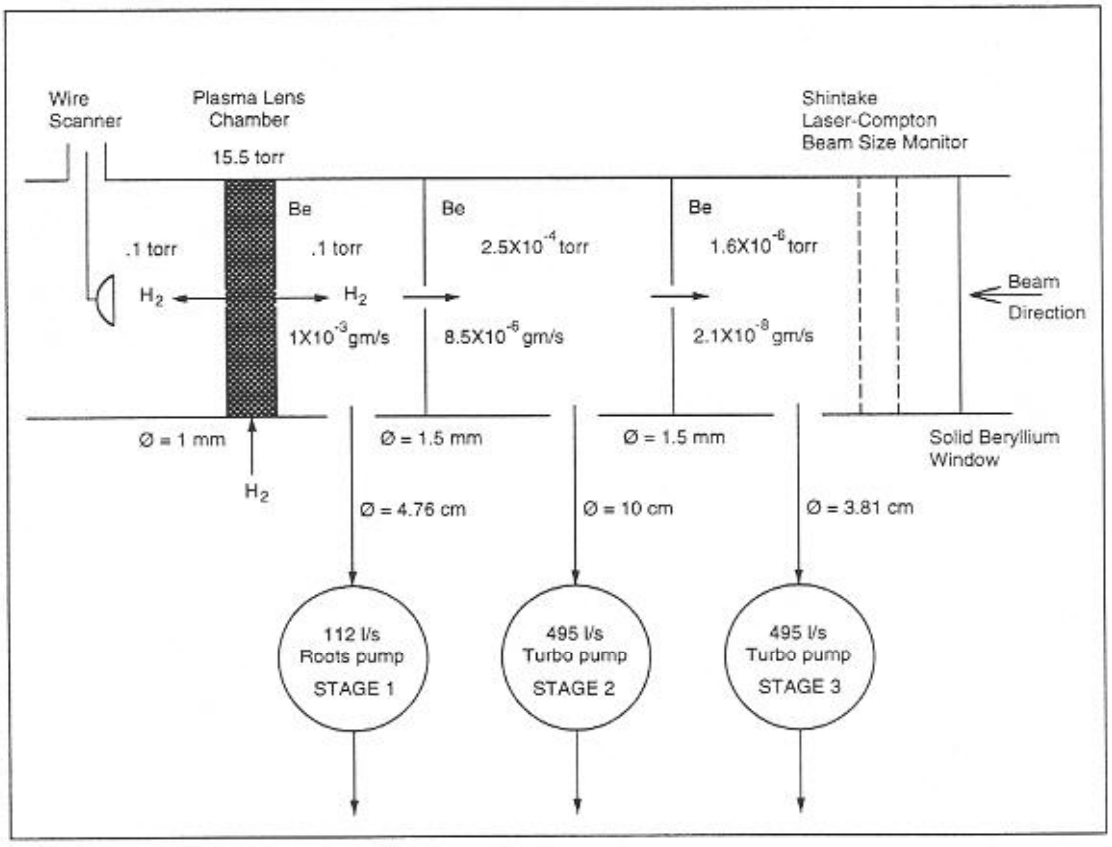

Figure 10: Differential Pumping System
The complete scheme consists of two of the system shown.

dimensions designed so that they will give the particle beam a clearance of at least 10σ for all FFTB operations as well as the plasma lens experiment. The differential pumping scheme is summarized in Figure 10.

Since vibrations from vacuum pumps must be kept to a minimum, only the turbo molecular pumps are connected directly to the plasma lens apparatus. Turbo molecular pumps have typical vibration amplitudes of less than 20 nm and can be reduced to less than 1 nm with the addition of vibration isolators at the inlet ports. The backing pumps for the turbo molecular pumps must be located off the plasma lens experiment platform.

Exhaust from the backing pumps will be vented outside the FFTB tunnel through a closed collection system. With the small amount of hydrogen involved, safety for the systems should not be a problem.

PROGRAM SUMMARY

The plasma lens experiment we intend to perform will serve to characterize plasma focusing devices, and if successful, will lead to practical applications at NLC and future linear colliders.

It is estimated that the installation and alignment at the FFTB will take about two months. All systems and components will then require approximately three weeks to be tested and calibrated. The plasma lens experiment will need 21 8-hour shifts of beam time to complete. The estimates are summarized in Table 2.

The primary goal in our experiment is to study the focusing of high energy and high density particle beams by plasma lenses of various densities. This experiment will establish the plasma lens as a compact, simple and economical add-on device for luminosity enhancement in linear colliders. Furthermore, the total compensation of beam self-fields by the plasma can be of interest for beamstrahlung suppression in future linear colliders, and for suppression of beam-beam tune-shifts in circular coliders.

Case	Description	Plasma	Beam Size Monitor	Shifts
Install	Installation & Alignment	—	—	two months
Check	All Systems & Components Check	—	—	three weeks
A	underdense lens, round beam focusing	laser ionized	wire scanner	7
B	overdense lens, round beam focusing	laser ionized	wire scanner	7
C	total compensation of beam fields	laser ionized	wire scanner	7

Table 2: Estimated Time Requirement.
Unless stated otherwise, shifts are in 8-hour units.

APPENDIX A

DETECTOR BACKGROUNDS FROM A PLASMA LENS AT NLC

A potential application of a plasma lens is its use as a final focusing device to increase the luminosity of a future high energy e^+e^- collider. However, the implementation of a plasma lens near a particle detector in such a collider requires that the presence of the plasma will not introduce serious backgrounds in the detector as a consequence of beam-plasma interactions. We do not consider the effect of plasma chamber material near the final focus. It will be possible to produce a plasma by injecting gas through a supersonic nozzle (see Appendix B) into the beam pipe, so that no material needs to be introduced close to the beam. Here we identify different sources of such backgrounds, calculate their event rates from the elementary interaction processes, and evaluate their effects on the major parts of a hypothetical Next Linear Collider (NLC) detector. For plasma lens parameters which give a factor of six enhancement of the luminosity, and using the NLC design for beam parameters as a reference, we find that the background yields are high, but manageable, assuming present and anticipated detector technology.

A.1 Choice of Plasma Lens Parameters

The background yield depends on both the beam and plasma lens parameters. For the former, we take the initial NLC beam energy of $E_{beam} = 250$ GeV, and $N = 0.65 \times 10^{10}$ particles per bunch, with $n_b = 90$ bunches in a bunch train.

For the flat beams of an NLC, with rms beam sizes $\sigma_x = 300$ nm, $\sigma_y = 3$ nm, and $\sigma_z = 100$ μm, it will be difficult to focus further in y. However, in the x-direction there is some possibility of improvement, as will be shown here.

As an example, we consider then a plasma lens beginning at $s_0 = -1$ cm from the final focus in absence of the lens, with a density $n_p = 2 \times 10^{18}$ cm^{-3}. Such a lens would have a focusing strength $K = 2\pi r_e n_p/\gamma \approx 7.24$ cm^{-2}. At the entrance to the lens, the NLC beta functions are changed from their value at the focus in the absence of a lens, $\beta^*_{x0} = 10$mm, $\beta^*_{y0} = 100$ μm, to

$$\beta_{x0} = \beta^*_{x0}\left(1+\left(\frac{s_0}{\beta^*_{x0}}\right)^2\right) = 1.01 \text{ cm}, \tag{A.1}$$

$$\beta_{y0} = \beta^*_{y0}\left(1+\left(\frac{s_0}{\beta^*_{y0}}\right)^2\right) = 1.01 \text{ cm}. \tag{A.2}$$

The differential equation for the beta function in the plasma lens as a function of the distance s along the beam line, $\beta''' + 4K\beta' + K'\beta = 0$, can be solved with the initial conditions (matching β, β' at $s = s_0$, the entrance to the plasma lens), yielding

$$\beta = \frac{\beta_0}{2} + \frac{1}{2K\beta^*_0} + \left(\frac{\beta}{2} - \frac{1}{2K\beta^*_0}\right)\cos[\nu(s+s_0)] - \frac{2d}{\nu\beta^*_0}\cos[\nu(s+s_0)] , \tag{A.3}$$

where $\nu = 4K$. We chose the thickness of the lens to be

$$\ell = \frac{\pi/2}{\sqrt{4K}} \approx 0.3 \text{ cm} . \tag{A.4}$$

The maximal reduction in β* can be found to be[36]

$$\frac{\beta^*}{\beta^*_0} = \frac{1}{1+K\beta^*_0(\beta_0-\beta_1)} , \tag{A.5}$$

where β_0, β_1 are the beta functions at the entrance and exit of the plasma lens, respectively. With the parameters given, one finds $\beta_x^* / \beta_{x0}^* = 1/8.5$, and the corresponding $\beta_y^* / \beta_{y0}^* = 1/4.9$, is smaller, as expected. The factor by which the luminosity increases, given by the square roots of these ratios of beta functions, thus can be as high as 6.5.

Note that the plasma lens parameters chosen above serve only as an illustration and are not necessarily optimized. However, they motivate the choice of the product of plasma density and plasma length, $n_p \ell = 0.6 \times 10^{18}$ cm^{-2} as appropriate for a study of backgrounds produced by a plasma lens at the NLC.

Here we consider only the use of a plasma lens as a device to focus one beam just before the interaction point. Focusing both beams would, of course, double the effect. One could also imagine having a suitably shaped plasma at the interaction point itself.

A.2 Sources of Backgrounds

Background particles produced by a plasma lens are of three types, namely, electrons and/or positrons, hadrons, and photons. These particles originate from different elementary physical processes underlying the interactions of the incoming electron or positron beam with the plasma of the lens located near the interaction point. In this section, we outline all the processes responsible for the various sources of backgrounds[37]. Their cross sections and angular distributions are calculated in the next section. From these results, the number of background particles can be determined for certain machine parameters. Using NLC as an example, the prospect of the application of plasma lenses with acceptable backgrounds in future linear colliders is examined in a subsequent section.

Electrons: Electrons and positrons arise from the scattering of the e^+ or e^- beam with the electrons of the plasma. The processes for producing electrons and positrons are: Bhabha scattering,

$$e^+ e^- \rightarrow e^+ e^-,$$

Møller scattering,

$$e^- e^- \rightarrow e^- e^-,$$

elastic scattering,

$$e\ p \rightarrow e\ p,$$

and inelastic scattering,

$$e\ p \rightarrow e\ X.$$

Hadrons: The hadronic backgrounds come from the elastic and inelastic scattering of the e^+ or e^- beam, and also from the inelastic scattering of photons (from synchrotron radiation and bremsstrahlung), with the protons in the plasma. Hadrons are produced by elastic scattering,

$$e\ p \rightarrow e\ p,$$

and inelastic scattering,

$$e\ p \rightarrow e\ X,$$

$$\gamma\ p \rightarrow X.$$

Photons: Photon backgrounds from a plasma are produced by Compton scattering,

$$e\ \gamma \rightarrow e\ \gamma.$$

Three mechanisms produce the incident photons: synchrotron radiation at the final focus quadrupole, synchrotron radiation as a consequence of plasma focusing, and bremsstrahlung of the e^+ or e^- beam in the plasma. These photons are then scattered by

plasma electrons into large angles. Note that all detectors at e^+e^- colliders have to cope with photon backgrounds generated by synchrotron radiation scattering off masks or similar structures, which is not considered here.

A.3 Cross Sections and Event Rates

The cross section of an electron or a photon scattered by the plasma for a particular process is calculated by integrating its angular distribution

$$\sigma = \int_{\theta_c}^{\pi-\theta_c} \frac{d\sigma}{d\Omega} d\Omega \ , \tag{A.6}$$

where θ_c is the angular cut for the scattered particles into the detector, which is taken to be 150 mrad in our calculations. The number of scattered particles N_s for a bunch train is then given by

$$N_s = n_b L \sigma \ , \tag{A.7}$$

where n_b is the number of bunches in a bunch train, and L is the beam-plasma luminosity per bunch crossing, respectively. The beam-plasma luminosity is given by

$$L = N n_p \ell \ , \tag{A.8}$$

where N is the number of particles in a bunch, n_p is the plasma density and ℓ is the thickness of the plasma. With the beam and plasma lens parameters of the previous section, the beam-plasma luminosity L is then 3.9×10^{27} cm^{-2}. For an anticipated NLC luminosity of $L_{NLC} = 6 \times 10^{33}$ cm^{-2}s^{-1}, the beam-beam luminosity per bunch crossing, $L_{NLC}/(180 n_b)$ is 3.7×10^{29} cm^{-2}, which is two orders of magnitude larger than the beam-plasma luminosity. For a bunch train of $n_b = 90$ bunches, $n_b L = 3.51 \times 10^{29}$ cm^{-2}.

While the energy of the electrons in the beam is monochromatic, the energy of the photons incident on the plasma lens is not. The photons originating from the final focus

quadrupole and the plasma focusing follow the synchrotron radiation spectrum, while those from bremsstrahlung in the plasma follow the Weizsäcker-Williams spectrum. Thus the photon distribution can be written as

$$n_\gamma(y) = n^p_{SR}(y) + n^q_{SR}(y) + n_{Brem}(y) \ , \qquad (A.9)$$

where $y = E\gamma/E_{beam}$ is the ratio of the photon energy to the beam energy, $n_\gamma(y)$ is the total photon spectrum, and $n^p_{SR}(y)$, $n^q_{SR}(y)$, and $n_{Brem}(y)$ are the contributions from plasma lens focusing, quadrupole focusing, and bremsstrahlung respectively. The synchrotron radiation spectrum from a focusing system can be approximated by the expression[38]:

$$n^i_{SR}(y) = \frac{1}{\pi}\Gamma(\frac{2}{3})(\frac{\alpha d_i}{\sqrt{3}\gamma\lambda\!\!\!^{-}_e})(3\Upsilon_i)^{2/3}y^{-2/3} \ , \quad 0 \le y \le \Upsilon_i \ , \quad i = p,q \ . \qquad (A.10)$$

Here $\lambda\!\!\!^{-}_e$ is the electron Compton wavelength, γ is E_{beam}/m_ec^2, d_i is the length of the focusing element (d_q = 1 m for a quadrupole and $d_p = \ell$ = 3 mm for a plasma lens), and Υ_i is $2E^i_c / 3E_{beam}$, where E^i_c is the synchrotron radiation critical energy. For $y > \Upsilon_i$, the synchrotron radiation power is exponentially small and is neglected here. For a final focus quadrupole, $\Upsilon_q \sim 1 \times 10^{-5}$ and $E^q_c \sim 2.5$ MeV. For the plasma lens considered here, Υ_p is about 0.2 and $E^p_c \sim 50$ GeV.

The bremsstrahlung spectrum from beam electrons scattered in the plasma is given by the Weizsäcker-Williams spectrum[39]

$$n_{Brem}(y) = \frac{2\alpha}{\pi y}[\ln 2.246 + \ln\frac{m_p}{m_e} - \frac{1}{2} - \ln y] \ , \qquad (A.11)$$

where m_p and m_e are the proton and electron masses, respectively. The angular distribution of the cross section for each Compton process, after taking the photon spectrum into account, is then given by

$$\frac{d\sigma}{d\Omega} = \int_0^{y_0} \frac{d\sigma(e\gamma \to e\gamma)}{d\Omega} n(y)dy \ , \qquad (A.12)$$

Background Source	Cross Section (cm^{-2})	Vertex Detector	Drift Chamber
Bhabha and Møller	0	0	0
Elastic ep: e	0.103×10^{-45}	negligible	negligible
p	0.613×10^{-39}	negligible	negligible
Inelastic ep: e	0.132×10^{-33}	negligible	negligible
charged hadrons	0.396×10^{-29}	0.018	0.018
Inelastic γp: charged hadrons	0.372×10^{-28}	0.12	0.12
Compton from quadrupole	0.995×10^{-25}	138 γs	174 γs
Compton from plasma focusing	0.548×10^{-25}	66 γs	120 γs
Compton from bremsstrahlung	0.119×10^{-24}	36 γs	18 γs

Table 3: Summary of Background Sources from a Plasma Lens in NLC. Calculations are for per bunch crossing. Each bunch has 0.65×10^{10} particles. The plasma lens has a density of 2×10^{18} cm^{-3} and a thickness of 3 mm

where n(y) is either the synchrotron radiation or the bremsstrahlung spectrum, and y_0 is the value above which radiation can be neglected, which is approximately 1.5×10^{-5}, 0.15 and 1 for quadrupole focusing, plasma focusing, and bremsstrahlung in the plasma, respectively.

The integrated cross sections and backgrounds from the different processes are summarized in Table 3. We now discuss in more detail the production of each type of background particle.

Electrons: The number of particles scattered into the detector depends on the angular acceptance, which is taken to be 150 mrad to π - 150 mrad from the incident beam direction. When a 250 GeV electron or positron hits an electron at rest, the scattered particles go in the forward direction within a cone of very small opening angle about the direction of the incoming electron. Thus we expect a very small number of electrons scattered into the detector when a beam passes through the plasma lens. Electron

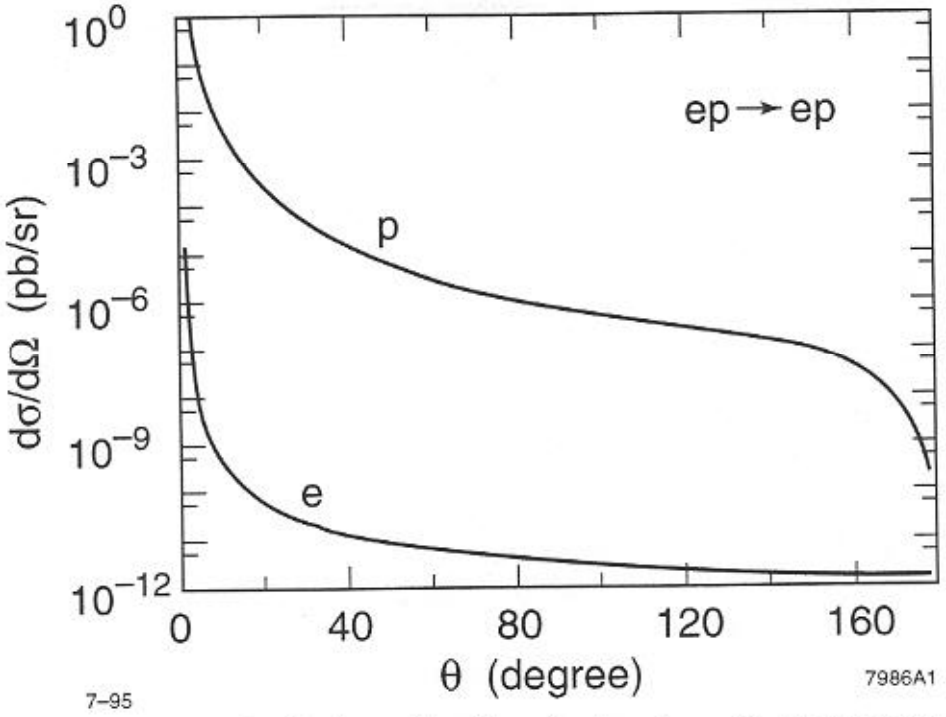

Figure 11: Angular Distributions of the Cross Sections for ep Elastic Scattering. The cross sections are in the laboratory frame. The energy of the incoming electron is 250 GeV and the proton is at rest.

backgrounds are essentially zero for Bhabha and Møller scatterings, since the scattered particles come out within the cone specified by our angular cut.

The angular distributions of the cross sections of the electrons and protons produced by elastic ep scattering are shown in Figure 11. The cross section for electron production peaks highly in the forward direction. The total cross section for the imposed angular cut is 0.103×10^{-45} cm^{-2}, and hence, the contribution to the electron sources is negligibly small.

The angular distribution of the scattered electrons for inelastic ep scattering can be obtained by integrating the following differential distribution[40] over energy:

$$\frac{d\sigma}{dE' d\Omega} = \frac{\alpha^2}{4E^2 \sin^4 \frac{\theta}{2}} \{W_2(\nu, q^2)\cos^2 \frac{\theta}{2} + 2W_1(\nu, q^2)\sin^2 \frac{\theta}{2}\} . \qquad (A.13)$$

Here E and E' are the incoming and outgoing electron energies respectively, $\nu = E - E'$, q^2 is the momentum transfer squared, and α is the fine structure constant. The parametrizations of the structure functions $W_1(\nu,q^2)$ and $W_2(\nu,q^2)$ are taken from Kwiecinski *et al.*[41]. The angular distribution of the cross section for inelastic ep scattering is shown in Figure 12(a). Again, we see that the cross section peaks highly in the forward direction. The total cross section is 0.132×10^{-33} cm^2, which gives 46×10^{-6} electrons for a bunch train. Hence it can be concluded that the electron backgrounds due to the presence of a plasma lens can be neglected.

Hadrons: While the electrons essentially move in the forward direction, the protons from ep elastic scattering are scattered into larger angles. In Figure 11 we see that the differential cross section is a few orders of magnitude bigger than that for the electrons. Nevertheless, the integrated cross section is 0.613×10^{-39} cm^2 and hence the contribution to the proton sources is negligibly small.

For inelastic ep scattering, the initial state proton can disintegrate into other particles. In order to properly take this effect into account we use HERWIG[42] to simulate the inelastic ep reactions of 250 GeV electrons with protons at rest. The differential distribution of charged hadrons as a function of scattering angle is shown in Figure 12(b) which shows again that the former peaks at small angles. The total cross section for the angular cut of 150 mrad is found to be 0.396×10^{-29} cm^2, which corresponds to about 1.4 charged hadrons for a bunch train at NLC energy. Thus, we expect the hadronic backgrounds from ep scattering will not pose problems to any component of a NLC detector.

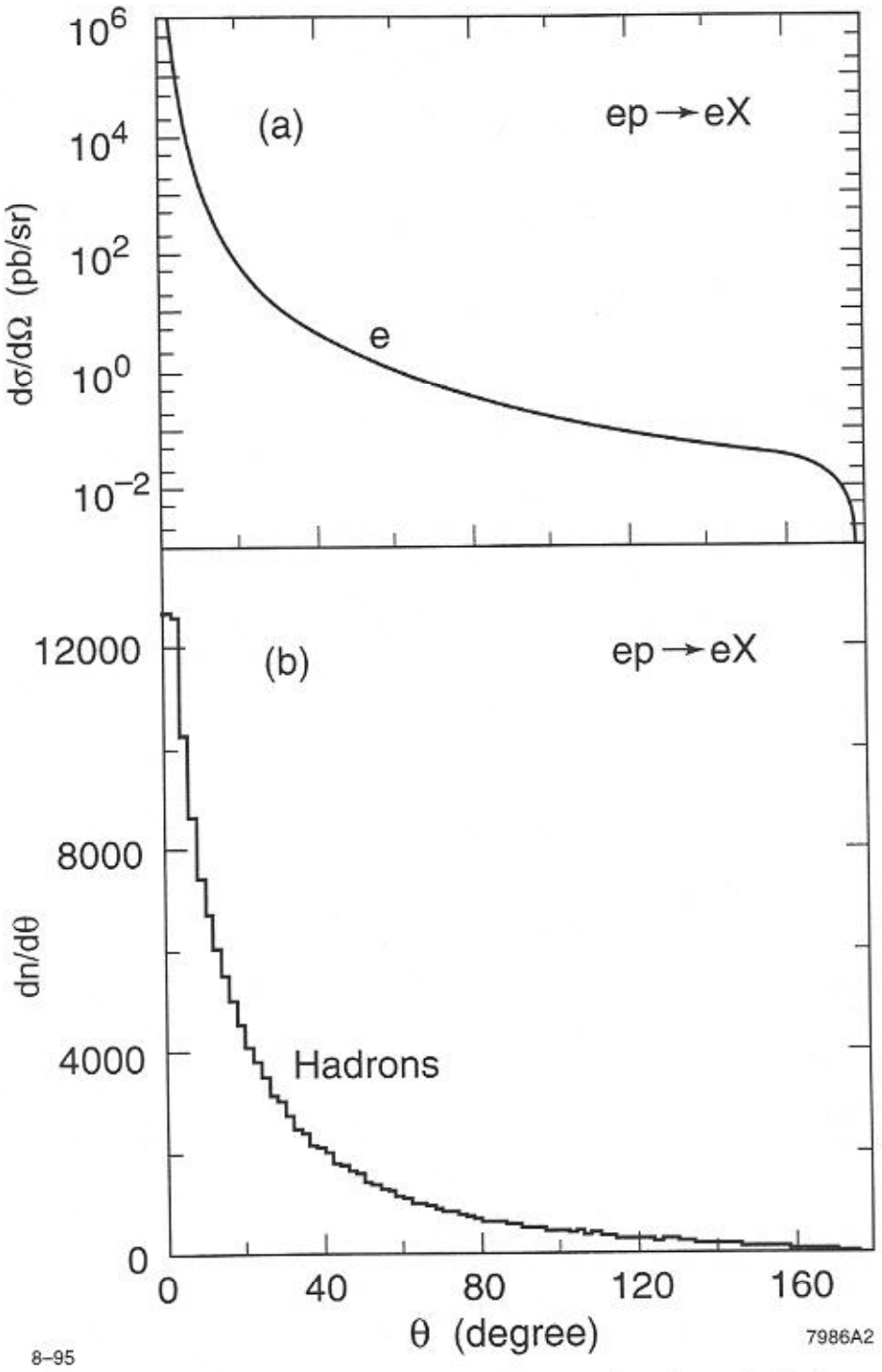

Figure 12: Angular Distributions of the Cross Sections for ep Inelastic Scattering

In (a), the cross section in the laboratory frame is shown. HERWIG angular distribution of charged hadrons for 20,000 events is shown in (b). The total cross section is normalized to 1.02×10^7 pb.

For inelastic γp scattering, where the photon originates from one of the mechanisms mentioned earlier, we found from HERWIG simulations that the cross section does not vary sensitively with the incoming photon energy. Hence, we considered a monochromatic photon of 10 GeV interacting with a proton at rest for estimating the cross section. The integrated cross section is found to be 0.372×10^{-28} cm^2, which is about eight times larger than that of the ep inelastic scattering. This corresponds to 13 charged hadrons for a bunch train, and hence the background is still very small.

Photons: The photon backgrounds for the Compton process from the three photon sources depend on the photon spectrum. When the photon energy is much greater than the electron rest mass, the Compton cross section has a peak in the forward direction. When the photon energy is comparable to or less than the electron mass, the scattering is reduced to Thomson scattering and the angular dependence of the cross section varies as a dipole distribution. The angular distributions of the cross sections of the Compton process from the three photon sources are shown in Figure 13. The bremsstrahlung spectrum is very soft and the angular distribution of this process is quite flat: it looks like a dipole distribution. The typical energy of the photon for synchrotron radiation from final quadrupole focusing is still small (of the order of 1 MeV) and hence, the distribution does not vary drastically with angle although it peaks moderately in the forward direction. Plasma focusing is much stronger than quadrupole focusing and the photon spectrum is expected to be harder with the typical energy on the order of 10 GeV. The cross section peaks in the forward direction and then drops rapidly at large angles. The total number of photons of all energies for a bunch train is ~96,000, or about 1070 for a single beam crossing. The photon backgrounds from γp inelastic scattering are in general a few orders of magnitude smaller than those from Compton scattering, and hence can be neglected.

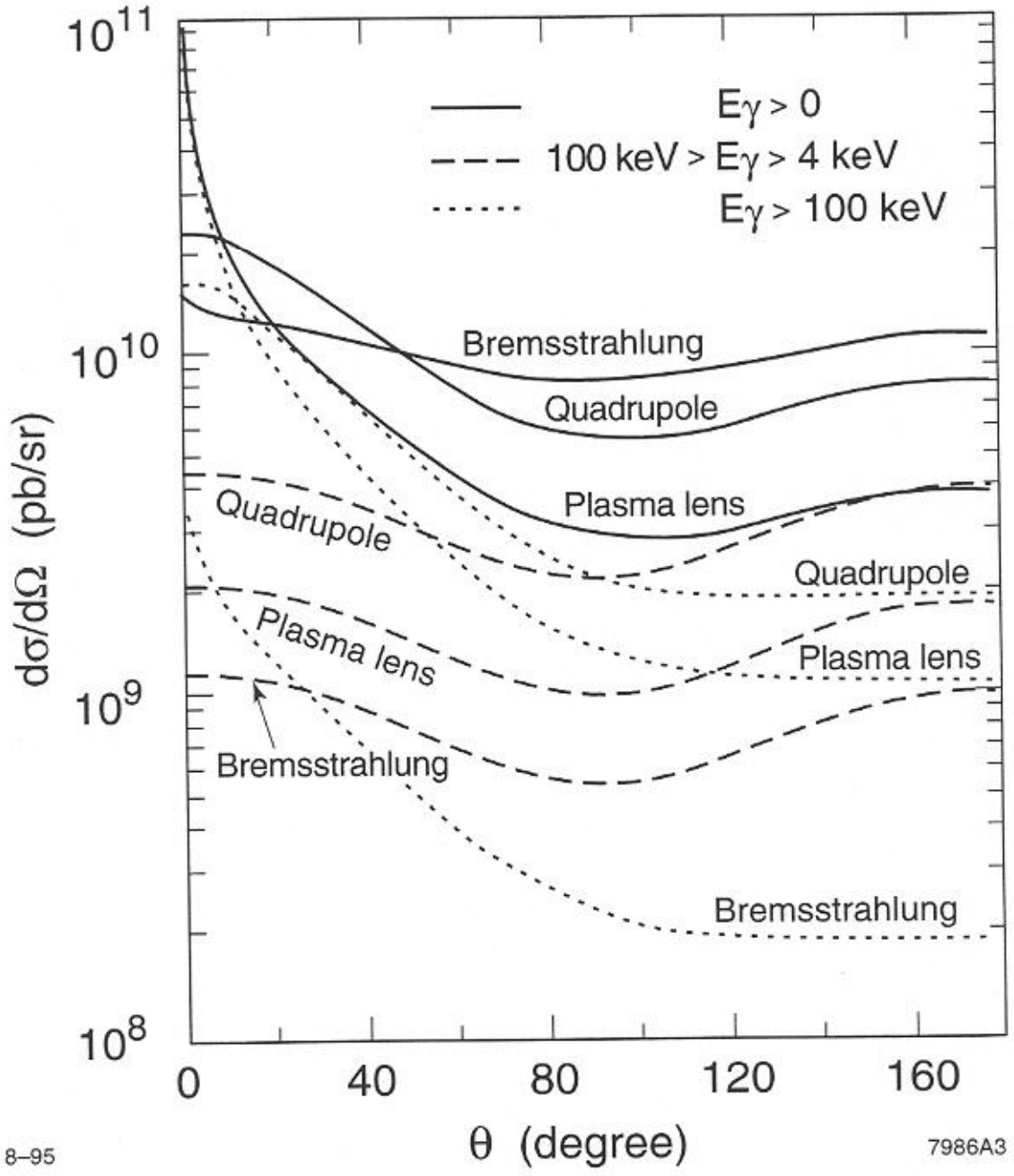

Figure 13: Angular Distributions of the Compton Cross Sections from Photon Sources The sources are bremsstrahlung in plasma, quadrupole focusing, and plasma lens focusing. The solid lines are for the whole energy range, the dashed lines for the energy range between 4 keV and 100 keV (relevant for the vertex detector), and the dotted lines for energy greater than 100 keV (relevant for the drift chamber).

A.4 Detector Backgrounds

As discussed in an earlier section, the leptons and hadrons scattered into the fiducial volume of a detector can be neglected.

The photons created by the different mechanisms calculated cover a wide range of energy. Different components of future linear collider detectors are sensitive to certain energy windows of the energy spectrum of the outcoming photons. We now consider the photon backgrounds in a vertex detector, a drift chamber or TPC, and a calorimeter of an idealized NLC detector.

Vertex Detector: A brief description of the general characteristics of a pixel-based vertex detector for the NLC can be found in the report by Damerell[43].

A minimum ionizing charged particle will deposit 7.75 keV and generate about 2,100 electron-hole pairs in the, say, 20 μm thick active silicon of a vertex detector. Photons above 50 keV, for example, are unlikely to convert in the very thin structure of a barrel vertex detector, which is expected to have a thickness of as little as 0.11% of a radiation length[43]. Thus, to be conservative, background photons of energies between, say, 4 keV and 100 keV need to be considered here. With these energy cuts, the number of background photons for the vertex detector is 21,600 for a bunch train, or 240 per single beam crossing, compared with 96,000 photons per bunch train at all energies. If one lowers the lower energy cut to 1 keV (280 electron-hole pairs), close to the noise limit of about 250 pairs, the number of relevant photons increases only to 300 per single beam crossing or 27,000 per bunch train.

The angular distributions of the cross sections from different mechanisms are shown in Figure 13 and they are dominated by Thomson scattering because of the relatively small energies. The cross section from bremsstrahlung photons is reduced by almost an

order of magnitude because of the cut at the lower end of the soft Weizsäcker-Williams spectrum. The cross sections from quadrupole and plasma focusing photons are roughly reduced by a factor of three.

For a vertex detector barrel with a radius of 2.5 cm and with a length of 33 cm covering angles greater than 150 mrad ($|\cos\theta| \leq 0.99$), the density of photon tracks per unit surface area is ~$0.42/mm^2$ for a bunch train, which is about 50% of the acceptable occupancy of ~$1/mm^2$. Even at the noise limit (1 keV lower cut), the occupancy remains below 60% of the value considered acceptable. Note that the choice of $|\cos\theta| \leq 0.99$ for the vertex detector is very generous. The number of background photons will be further reduced if the angular coverage is limited to, for example, $|\cos\theta| \leq 0.90$.

Drift chamber: The next layer in the detector may well be a large drift chamber or TPC with about 10,000 sense wires. Such a drift chamber can easily tolerate 100 random background hits (1% occupancy). Assuming a 1% conversion probability, this allows for 10,000 incident photons. Photons of very small energies, say ≤ 10 keV, will be absorbed by the beam pipe and can be ignored. The conversion products of photons of less than, say 100 keV, will not form track segments. In a typical magnetic field they will form tight loops and deposit their energy locally. Proper design of the readout should account not only for the charge distribution typical of minimum ionizing particles, but also for the sometimes large local depositions of energy from converting photons. Thus we need only to consider photons of energy greater than 100 keV scattered into the drift chamber.

The angular distributions of the cross sections above 100 keV are shown in Fig. 3. They all peak in the forward direction as a result of the hard photon spectra from all the mechanisms. The total number of background photons with energy above 100 keV and scattering angle greater than 150 mrad is about 28,200 per bunch train, which corresponds

to a 2.8% occupancy of the drift chamber. Notice that we integrated the background over a whole bunch train. By the time NLC is built, we expect that progress in tracking technology will allow a better separation of tracks from adjacent bunch crossings, such that only the background from a few adjacent bunch crossings (instead of 90) needs to be considered.

Calorimeter: As mentioned earlier, leptons and hadrons will not be scattered into the main part of a detector in sufficient numbers to cause a problem for the calorimeter of a hypothetical NLC detector. Photons of very low energies will have been absorbed by the beam pipe, drift chamber walls, and similar structures before reaching the calorimeter. A typical calorimeter can possibly see energies as low as a few MeV. However, for any actual analysis, a cut is made removing clusters in a calorimeter with a total energy below, say, 100 MeV. Our simulation shows that of the total flux per bunch train of about 96,000 photons of all energies in the angular region with $|\cos\theta| \leq 0.99$, none have an energy above 100 MeV, and about 7,440 per bunch train, or ~38 per single beam crossing, have an energy between 1 and 100 MeV. While some of the latter might be seen in the innermost layer of electromagnetic calorimetry, they do not present a problem and are easily removed by a cluster cut, if isolated. The energy added by them to a shower created by a high energy particle or jet is negligible compared to the intrinsic resolution of a typical calorimeter. Calorimeter backgrounds might also be attributed to individual bunch crossings by the use of scintillation counters or similar fast timing devices, so that again integration of the backgrounds over a bunch train is excessively conservative.

A.5 Summary

We summarize our background calculations in Table 3, which shows the various cross sections and particle fluxes for a single bunch crossing from the different background sources. As mentioned earlier, we have taken the NLC parameters as a reference. We have further assumed that the resolution time for the detector is much longer than 1.4 ns, the separation between successive bunches in a bunch train, but less than the ~5 ms separation between bunch trains. Therefore, to be conservative, we integrated in our discussion the events over a train of 90 bunches for a total time span of ~125 ns.

We have estimated only the sources of backgrounds from a plasma lens for a generic particle detector but did not consider here the additional sources of backgrounds that are common to any NLC detector, such as those due to beam scrapings or synchrotron radiation scattering off masks or similar structures. The discussion in Section A.4 and Table 3 show that all the main components of the detector should survive the plasma lens induced backgrounds. Thus the implementation of a plasma lens for luminosity enhancement in high energy e^+e^- collisions is feasible without hampering the normal performance of the detector. Nevertheless, taking the present calculations as input, a more detailed and reliable estimate of the detector response to these background particles should be carried out by a *bona fide* detector simulation.

APPENDIX B

SUPERSONIC GAS NOZZLE FOR FUTURE PLASMA LENS APPLICATIONS

In an effort to further reduce the amount of hardware for a the plasma lens located deep inside a high energy collider detector, and hence to minimize high energy background events, a supersonic hydrogen gas nozzle is being developed for use with future plasma lens applications in mind. In addition to minimizing potential background events, the gas jet approach to a plasma lens has practical advantages during initial beam tuning.

B.1 Nozzle Design

The axis-symmetric supersonic gas nozzle was designed using a one-dimensional gas model that assumes an ideal gas in steady-state, isentropic flow[44]. The design parameter is chosen to be five times the required molecular density required for a plasma with electron density of 10^{18} cm^{-3}, which for hydrogen is $N_e = 2.5 \times 10^{18}$ cm^{-3}, at the nozzle exit. The inlet gas temperature is $T_o = 300$ K, and the pressure is $P_o = 2{,}000$ psia. The Mach number at the nozzle exit is given by

$$M_e = \left[\frac{2}{\gamma - 1} \cdot \left[\left(\frac{\rho_o}{\rho_e} \right)^{\gamma - 1} - 1 \right] \right]^{\frac{1}{2}}, \qquad \text{(B.1)}$$

where ρ_o and ρ_e are the mass densities at the entrance and exit of the nozzle respectively, and $\gamma = 1.4$ is the ratio of the specific heats for diatomic molecules.

The 40 μm throat diameter and the 10° opening angle of the diverging section are chosen based on previous experiment[45] with similar supersonic gas nozzle. For a gas jet

with a diameter of order 1 mm, a nozzle with throat diameter of approximately d_t = 40 μm is required. The required exit area of the nozzle is then given by

$$A_e = \frac{\pi d_t^2}{4M_e} \cdot \left[\frac{1+(\frac{\gamma-1}{2}) \cdot M_e^2}{1+(\frac{\gamma-1}{2})} \right]^{\frac{\gamma+1}{2(\gamma-1)}} . \qquad (B.2)$$

The temperature of the gas at the exit is

$$T_e = \frac{T_o}{1+(\frac{\gamma-1}{2}) \cdot M_e^2} , \qquad (B.3)$$

and the velocity of the gas at the exit is

$$v_e = M_e \cdot \sqrt{\frac{\gamma R T_e}{m}} , \qquad (B.4)$$

where R is the gas constant and m is the molecular weight. The mass flow rate through the exit plane is

$$\Phi = \rho_e v_e A_e . \qquad (B.5)$$

With a fixed nozzle geometry, the Mach number at the nozzle exit is fixed and the density at the exit can be controlled by varying the inlet, or stagnation pressure.

The molecular density, N_e, is five times the required value to compensate for the decreasing density with increasing distance from the nozzle exit. Assuming that the jet continues to expand for a short distance beyond the exit plane of the nozzle with the same 10° angle as the diverging section, it will reach a diameter of approximately 1 mm in a distance of about 5 mm. The molecular density will have fallen from 2.5 × 10^{18} cm^{-3} to 1.25 × 10^{18} cm^{-3}, but it remains ample for the plasma lens experiment.

It should be noted that by cooling the gas supply to the nozzle, the same density of 10^{18} cm^{-3} can be achieved with a lower stagnation pressure, and consequently a lower

mass flow rate. It is planned that liquid nitrogen pre-cooling of the hydrogen gas be used in the plasma lens experiment.

Although clustering[46] has not been considered, it is not expected to be a problem for uniform plasma formation. Typical cluster spacing is of order 10^{-7} m, which is a very small fraction of the length of the plasma lens.

B.2 Nozzle Fabrication

Production of a nozzle with 40 μm throat diameter and 10° conical taper is beyond the limits of conventional machining process. Yet compatible technologies such as micro-machining and electric discharge machining (EDM) are slow and costly.

As a result, a special procedure was developed to produce copper nozzles using conventional machining techniques combined with an extrusion process to achieve the final throat diameter. First, specially ground tapered drills are used to bore the 10° diverging

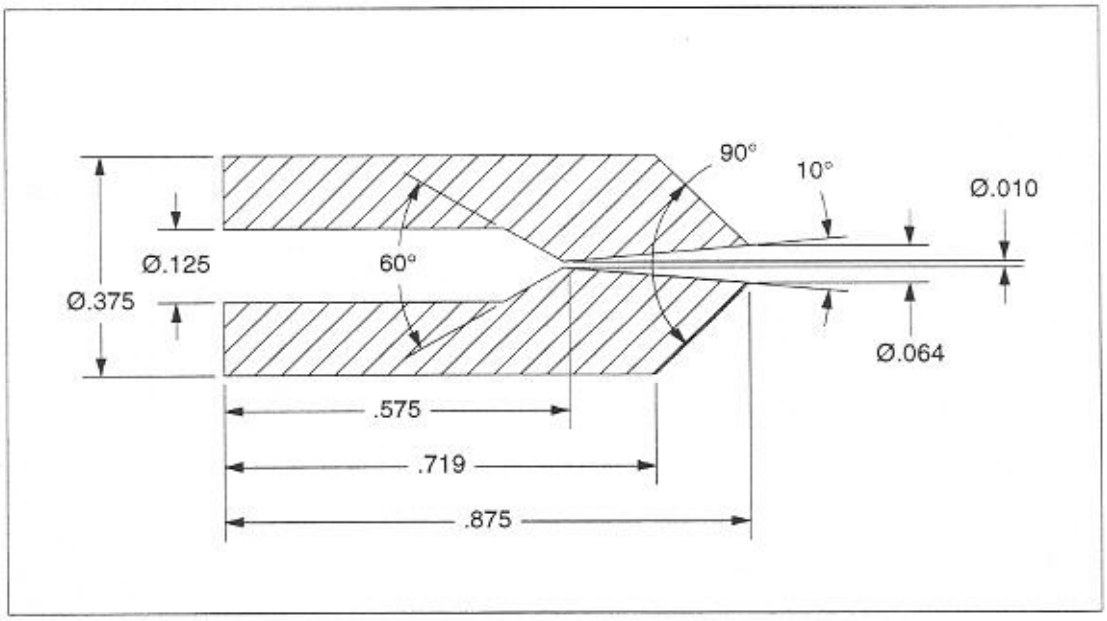

Figure 14: Supersonic Gas Nozzle Design Prior to Extrusion

section while a standard drill is used for the converging section. After the two sections are created, a small drill (about 0.2 mm in diameter) is used to break through and connect the two sections. Subsequently, the copper nozzle is then forced through a steel extrusion die to achieve a small throat diameter. The design of the nozzle before extrusion is shown as Figure 14.

The entire process of machining, extrusion, inspection and measurement with an optical comparator can be accomplished in approximately 8 hours. Virtually any throat diameter can be achieved by changing the inside and outside diameters of the nozzle before extrusion. The proper initial dimensions were determined empirically and after seven attempts a nozzle with a 70 μm throat diameter was produced for initial testing.

B.3 Initial Operation

During the plasma production test at the University of Rochester, preliminary testing of the supersonic gas nozzle was performed. Unfortunately, the best nozzle produced and available for testing has a 70 μm throat diameter, and the existing gas delivery system at the University of Rochester was certified to be operated safely at low pressure (less than 100 psia). Nonetheless, plasmas were created using the supersonic gas jet as the gas source and the densities were measured. The validity of the design of the supersonic gas nozzle is verified.

The supersonic gas nozzle was installed in the test chamber through an existing gas delivery system on top of the chamber (Figure 5). The gas line was coupled to a X-Y-Z positioner before entering the chamber, so that the supersonic gas nozzle attached to the end of the line can be moved in all dimensions relative to the laser. Xenon at a pressure of 40

psia was supplied to the nozzle through an electronic valve which was synchronized to open a short time before the firing of the laser.

The plasma density was determined by measuring the emitted recombination light with a photomultiplier tube (PMT). The arrangement and calibration were identical to the plasma production test. The nozzle was moved about relative to the laser using the X-Y-Z positioner so that the plasma densities at different parts of the jet can be measured.

Since the nozzle was operating at a pressure of 40 psia which is far lower than its designed operating pressure, the plasmas created were much less than 10^{18} cm^{-3}. However, the results can be compared with the calculated densities of the jet at the test conditions.

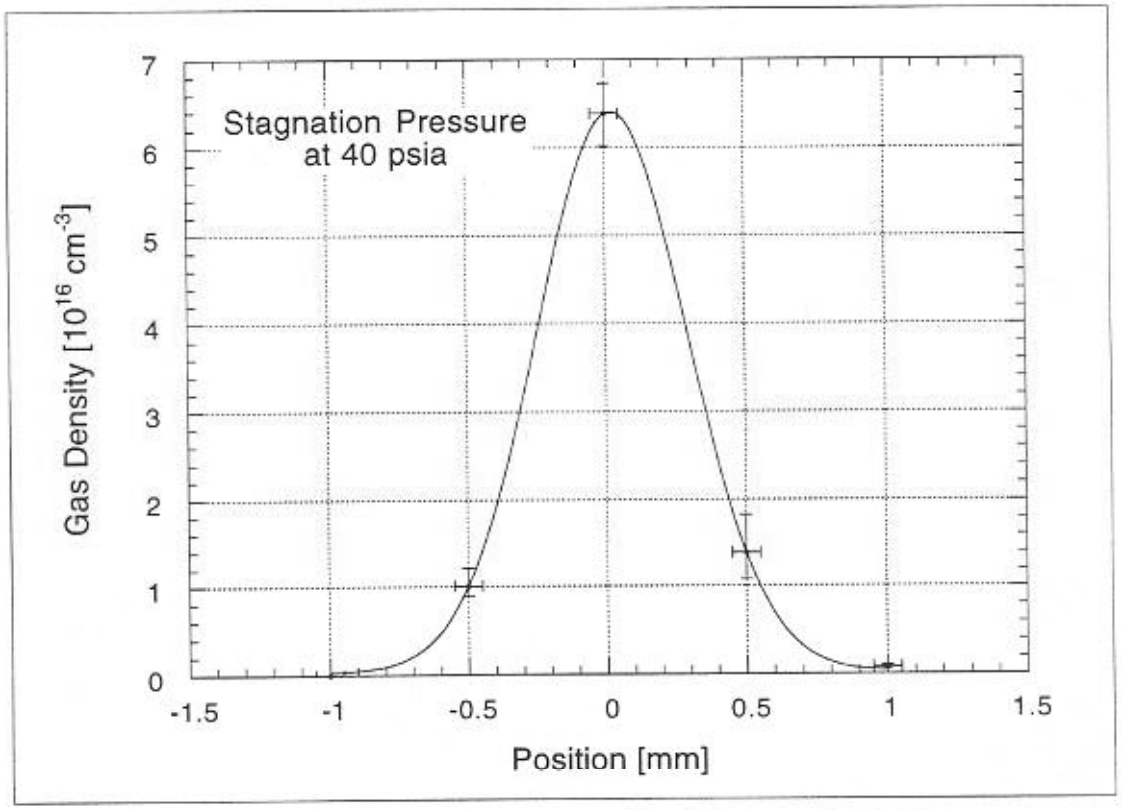

Figure 15: Transverse Density Profile of Supersonic Gas Jet

The transverse density profile of the supersonic gas jet at the exit of the nozzle is shown as Figure 15. Although the profile is shown as a Gaussian type for better visualization despite the limited amount of data in the figure, it most likely is not in actuality. The predicted gas density at the exit is 7.7×10^{16} cm^{-3}, while the measurement gives a density of 6.4×10^{16} cm^{-3}. The agreement is quite good given the simplicity of the model. The density obtained is even sufficient for performing underdense plasma lens tests at the FFTB.

The obtainable density should scale comfortably into the 10^{18} cm^{-3} range with a stagnation pressure of 2,000 psia. Hence, the nozzle is performing as the design model has predicted.

B.4 Summary

A continuous supersonic gas nozzle has been designed and tested as the plasma gas source. Initial testing of the nozzle at low pressure has proved the validity of the design model. The plasma density obtained in the initial test is even sufficient for underdense plasma lens (Case A) tests at the FFTB. With the nozzle operating at the designed stagnation pressure of 2,000 psia, a gas jet of density of order 10^{18} cm^{-3} should be obtainable.

A novel procedure has been developed to produce the nozzle using conventional machining techniques combined with an extrusion process. Although the procedure was developed empirically, the simplicity of it allowed nozzles to be manufactured efficiently.

REFERENCES

[1] W. Barletta *et al.*, "SLAC Proposal E-150," SLAC (1993).

[2] P. Chen, Part. Accel. **20**, 171 (1987).

[3] P. Chen, J. J. Su, T. Katsouleas, S. Wilks, and J. M. Dawson, IEEE Trans. Plasma Sci. **15**, 218 (1987).

[4] J. B. Rosenzweig and P. Chen. Phys. Rev. D **39**, 2039 (1989).

[5] P. Chen, S. Rajagopalan, and J. B. Rosenzweig, Phys. Rev. D **40**, 923 (1989).

[6] J. J. Su, T. Katsouleas, J. M. Dawson, and R. Fedele, Phys. Rev. A **41**, 3321 (1990).

[7] P. Chen, Phys. Rev. A **45**, R3398 (1992).

[8] P. Chen, K. Oide, A. Sessler, and S. Yu, Phys. Rev. Lett. **64**, 1231 (1990).

[9] K. Oide, Phys. Rev. Lett. **61**, 1713 (1988).

[10] J. B. Rosenzweig *et al.*, Phys. Rev. Lett. **61**, 98 (1988).

[11] H. Nakanishi *et al.*, Phys. Rev. Lett. **66**, 1870 (1991).

[12] G. Hairapetian *et al.*, Phys. Rev. Lett. **72**, 2403 (1994).

[13] P. Chen, J. M. Dawson, W. Huff, and T. Katsouleas, Phys. Rev. Lett. **54**, 693 (1985); R. D. Ruth, A. W. Chao, P. L. Morton, and P. B. Wilson, Part. Accel. **17**, 171 (1985).

[14] D. H. Whittum, A. M. Sessler, J. J. Stewart, and S. S. Yu, Part. Accel. **34**, 89 (1990).

[15] J. L. Cox, and W. H. Bennett, Phys. Fluids **13**, 182 (1970).

[16] P. Tenenbaum *et al.*, SLAC-PUB-6593 (1994).

[17] P. Chen, C. K. Ng, and A. W. Weidemann, SLAC-PUB-6941 (1995).

[18] P. Chen, T. Barklow, and M. Peskin, Phys. Rev. D **49**, 3209 (1994).

[19] S. Rajagopalan, D. B. Cline, and P. Chen, Nucl. Inst. Meth. A **355**, 169 (1995).

[20] P. Chen, A. Spitkovsky, and A. W. Weidemann, Int. J. Mod. Phys. A **11**, 1687 (1996).

[21] S. Heifets and T. Raubenheimer, CERN-CLIC-NOTE-324 (1996).

[22] G. Stupakov and P. Chen, Phys. Rev. Lett. **76**, 3715 (1996).

[23] P. Chen in "The Physics of Beams," Andrew Sessler Symposium, ed. W. A. Barletta, AIP Conf. Proc. **351** (1996).

[24] D. Betz, P. Chen, D. Cline, M. Gundersen, C. Joshi, T. Katsouleas, J. Norem, S. Rajagopalan, J. B. Rosenzweig, J. J. Su, and R. Williams, IEEE Part. Accel. Conf. Proc. 88-647453, 619 (1991).

[25] J. G. Heinrich *et al.*, "SLAC PROPOSAL E-144," (1991).

[26] S. Angst, D Strickland, D. D. Meyerhofer, S. L. Chin, and J. H. Eberly, Phys. Rev. Lett. **63**, 2212 (1989).

[27] D. Strickland *et al.*, Opt. Comm. **56**, 219 (1985).

[28] P. Maine, D. Strickland, P. Bado, M. Pessot, and G. Mourou, IEEE J. Quant. Elec. **24**, 398 (1988).

[29] Y. H. Chuang, D. D. Meyerhofer, S. Angst, H. Chen, J. Peatross, and S. Uchida, J. Opt. Soc. Am. B **8**, 1226 (1991).

[30] J. Sheffield, "Plasma Scattering of Electromagnetic Radiation," Academic Press, New York (1975).

[31] C. Field *et al.*, Nucl. Inst. Meth. A **295**, 279 (1990).

[32] W. P. Leeman *et al.*, Phys. Rev. A **46**, 1091 (1992).

[33] C. Darrow *et al.*, Phys. Rev. Lett. **69**, 442 (1992).

[34] L. A. Lompré *et al.*, J. Appl. Phys. **63**, 1791 (1988).

[35] J. F. O'Hanlon, "A User's Guide to Vacuum Technology," John Wiley & Sons, New York (1989).

[36] P. Chen, C. K. Ng, and S. Rajagopalan, Phys. Rev. E **48**, 3022 (1993).

[37] C. Baltay, "Backgrounds in SLD due to the Proposed SLC Plasma Lens," SLD Internal Note (1992).

[38] P. Chen, "Beamstrahlung and the QED, QCD Backgrounds in Linear Colliders," SLAC-PUB-5914 (1992); "Photon-Photon Collisions," ed. D. O. Caldwell and H. P. Paar, World Scientific, New York (1992).

[39] J. D. Jackson, "Classical Electrodynamics," John Wiley & Sons, New York (1975).

[40] F. Halzen and A. D. Martin, "Quarks and Leptons," John Wiley & Sons, New York (1984).

[41] J. Kwiecinski, A. D. Martin, R. G. Roberts, and W. J. Stirling, Phys. Rev. D **42**, 3645 (1990).

[42] G. Marchesini *et al.*, Comp. Phys. Comm. **67**, 465 (1992).

[43] C. J. S. Darmerell, "Vertex Detectors at Linear Colliders (Present and Future)," RAL Report 94-096 (1994).

[44] M. Sadd, "Compressible Fluid Flow," Prentice Hall, New Jersey (1985).

[45] J. Brolley, IEEE Nucl. Sci. **20**, 475 (1971).

[46] M. Macri, "Hadronic Physics at Intermediate Energy," Elsevier, Netherlands (1987).